

박 사 학 위 논 문

Emittance Evolution Process
in High Brightness Photo-Cathode RF Gun
with Focusing Solenoids

박 장 호 (朴 壯 皓)

물리학과 (가속기물리 전공)

포항공과대학교 대학원

2007년

솔레노이드 집속 전자석을 가진
고휘도 고주파 광전자 총의
에미턴스 전개과정에 관한 연구

Emittance Evolution Process in High
Brightness Photo-Cathode RF Gun
with Focusing Solenoids

Emittance Evolution Process
in High Brightness Photo-Cathode RF Gun
with Focusing Solenoids

by

Jangho Park

Department of Physics

POHANG UNIVERSITY OF SCIENCE AND TECHNOLOGY

A thesis submitted to the faculty of Pohang University of Science and
Technology in partial fulfillment of the requirements for the degree of
Doctor of Philosophy in the Department of Physics

Pohang, Korea

2006. 12. 8.

Approved by

In Soo Ko

Major Advisor

솔레노이드 집속 전자석을 가진
고휘도 고주파 광전자 총의
에미턴스 전개과정에 관한 연구

박 장 호

위 논문은 포항공과대학교 대학원 박사학위 논문으로 학위 논문
심사위원회를 통과하였음을 인정합니다.

2006 년 12 월 8 일

학위논문 심사위원회 위원장	고 인 수	(인)
위 원	남 궁 원	(인)
위 원	조 무 현	(인)
위 원	윤 무 현	(인)
위 원	황 정 연	(인)

DPH 박 장 호, Jangho Park, 솔레노이드 집속 전자석을 가진 고휘도
20033342 고주파 광전자 총의 에미턴스 전개과정에 관한 연구, Emittance
Evolution Process in High Brightness Photo-Cathode RF Gun with
Focusing Solenoids, Department of Physics, 2006, 97 pp. Advisor: 고
인 수 (In Soo Ko). Text in English

Abstract

A BNL GUN-IV type photocathode rf gun has been fabricated to use in Femto-second Electron Diffraction (FED), femto-second Far Infra-red Radiation (fs-FIR) facility, and X-ray Free Electron Laser (X-FEL) at the Pohang Accelerator Laboratory (PAL). The gun consists of a 1.6-cell cavity with a copper cathode, solenoids for beam emittance compensation, beam diagnostic components for beam characteristics and auxiliary systems. The dimension of the cavity that provides desired resonant frequency is determined by the SUPERFISH code for 2D dimension determination. Change of the resonant frequency due to laser ports, a pumping port, and a waveguide port on the cavity wall was estimated with Slater's perturbation theorem. The dimensions of the waveguide port for the magnetic coupling from the klystron to the gun cavity are finalized by a series of the cutting and measuring processes. Basic beam parameters are measured to confirm the successful fabrication of the photocathode RF gun system. Basic diagnostics for the beam include the beam spot size, the beam charge, the beam energy, and the beam emittance. The best performance of the beam energy and the

bunch charge of the photo-electron beam is measured as 3.7 MeV and 550 pC at the 30° laser injection phase, respectively. The rms beam spot size and the normalized rms transverse emittance of the beam are measured as 0.79 ± 0.042 mm and 1.72 ± 0.29 mm-mrad at 3.7 MeV beam energy with 300 pC beam charge at 30° laser injection phase, respectively. In addition to these results, measurements of the emittance evolution by the emittance meter are carried out. These experimental approaches in various beam conditions can lead proper experimental conditions for the PC RF gun commissioning using the fully emittance compensated beam. The experimental and the computational approaches of the emittance evolution and the compensation are introduced in this thesis.

CONTENTS

1	Introduction	1
2	Pohang Accelerator Laboratory X-ray Free Electron Laser and Its Pohang Photo Injector	5
2.1	Pohang Accelerator Laboratory X-ray Free Electron Laser (PAL XFEL)	5
2.2	The Pohang Photo-Injector (PPI) for the PAL XFEL	10

CONTENTS

3	Emittance Compensation Theory and Simulation	13
3.1	Introduction	13
3.2	Emittance definition	14
3.3	Theory of the emittance compensation	18
3.4	Simulation study of the photocathode RF gun	21
3.4.1	Simulation of the emittance evolution	21
3.4.2	Simulation of the beam dynamics in the cavity	25
4	RF Measurement and High Power Test	31
4.1	Cavity design	31
4.1.1	Determination of the cavity diameter	31
4.1.2	Modification of coupling coefficient	36
4.1.3	Beam dynamics simulation	37
4.2	Microwave characterizations	39
4.2.1	Measurement of the model cavity	39
4.2.2	Measurement of the cavity	42
5	Experimental Setup and Results	51
5.1	Photocathode RF Gun	51
5.2	Emittance Meter	58
5.3	Laser system	62
5.4	Experimental results	68

CONTENTS

5.4.1	Beam charge and quantum efficiency versus laser injection phase	68
5.4.2	Dark Current Measurement	76
5.4.3	Laser Injection Phase versus Energy	79
5.4.4	Measurements of the Transverse Emittance Evolution	81
6	Conclusion and Future Work	87
6.1	Conclusion	87
6.2	Future Work	88
6.2.1	Issues of the Beam dynamics Study	89
6.2.2	Issues of the Stability of the Photocathode RF Gun	90
	Reference	91
	Summary in Korean	
	Curriculum Vitae	
	Acknowledgments in Korean	

LIST OF FIGURES

2.1	The design layout of the PAL XFEL	9
2.2	The schematic diagram of the PPI for the PAL XFEL. The photo-cathode RF gun for PAL XFEL, a thermionic gun for injection of the Pohang Light Source, and a polarized electron source (PES) gun are separately installed on the PPI site	12
3.1	The phase space ellipse of the emittance	16

LIST OF FIGURES

3.2	The emittance evolution simulation by the PARMELA code. The normalized rms transverse emittance at the simulation with the proper matching condition is damped to minimum value. The thick line is the LCLS photo-injector model and the thin line is modified our photo-injector model	21
3.3	(a) The electric field in the cavity and (b) the magnetic field profile of the solenoids of the compensation and the accelerating column	23
3.4	The evolution of the rms beam spot size (a), (c) and the emittance (b), (d) with various magnetic field strength of the solenoid. The simulations are performed with a 120 MV/m and 90 MV/m accelerating field gradient and a 1 nC and 0.4 nC beam charge, respectively	24
3.5	The beam energy simulation in the cavity as a function of the laser injection phase. These simulations are performed under the condition of a 79 MV/m electric field at the cathode	26
3.6	The beam energy simulation in the cavity as a function of the laser injection phase. These simulations are performed under the condition of a 65 MV/m electric field at the cathode	27
3.7	The beam energy simulation in the cavity as a function of the laser injection phase. These simulations are performed under the condition of a 53 MV/m electric field at the cathode	28
3.8	The beam energy simulation as a function of the laser injection phase with various electric fields in the cavity	29

LIST OF FIGURES

4.1	Simulation with SUPERFISH 2D code to determine resonant frequencies: (a) Half cell, 2,855.77 MHz; (b) full cell, 2,870.02 MHz	33
4.2	Electric field drawing in the cavity at the o-mode (a) and the π -mode (b) using the SUPERFISH simulation	34
4.3	(a) The designed field profile of the solenoids with POSSION code, (b) the measured field profile with the field measurement device, (c) the designed electric field in the cavity, and (d) the simulation results for the normalized emittance evolution (dotted line), the beam size evolution (solid line), and the beam energy evolution (dashed line)	38
4.4	The photograph of the model cavity to check the tuning property of the gun cavity	39
4.5	(a) Network-analyzer measurement of the two resonant modes in the gun cavity and (b) transient response of the gun cavity to pulsed RF power. The mode separation is measured to be 3.4 MHz	41
4.6	The resonant frequency change as a function of the tuner depth on the cavity wall surface. Its relation is non-linear because different frequency effects are given by the magnetic field properties at different positions from the cavity wall surface	42
4.7	The measured microwave parameters: (a) the measured S_{11} parameter, (b) the measured VSWR chart, and (c) the Smith chart under the vacuum at room temperature (25 °C)	45

LIST OF FIGURES

4.8	The S_{11} measurement of the cavity under vacuum condition at the different temperature by the network analyzer: In the upper figure, the π -mode resonant frequency at the 25.0 °C is 2,856.25 MHz with 3.4 MHz mode separation. In the bottom figure, the π -mode resonant frequency at the 32.0 °C is 2,856.0 MHz with the same mode separation	46
4.9	The measured resonant frequency as a function of the temperature in the cavity. The temperature coefficient is measured -42.37 kHz/°C	47
4.10	Schematic diagram of the RF network of the photocathode RF gun. Symbol K means a klystron	48
4.11	Measurement of the resonant frequency with a directional coupler in the klystron waveguide at cavity cooling temperature with 32.0 °C	49
5.1	Schematic diagram of the gun test (GTS) at the PAL	53
5.2	Photograph of the gun test (GTS) at the PAL	54
5.3	The solenoid for the emittance compensation: (a) the measured field profile of the solenoid on axis, (b) the graph of the applied current on the solenoid vs. peak solenoid field, (c) schematic diagram of the solenoid field measurement device based on hall-probe measurement, (d) the photograph of the solenoid field measurement device	55
5.4	(a) The schematic diagram of the steering magnet inside of solenoid bore and (b) the graph of the applied current vs. measured magnetic fields of the steering magnet	56

LIST OF FIGURES

5.5	The spectrometer magnet for beam energy measurements: (a) The drawing of the spectrometer magnet, (b) the photograph of the spectrometer, (c) the graph of the applied spectrometer magnet current vs. beam energy based on the measured spectrometer field	57
5.6	The diagram of the emittance measurement setup for the measurement of the beam	60
5.7	The schematic diagram of the single slit plates and its holder (a). The slit width is 30, 40, and 50 μm , respectively. The photographs of the fabricated slit plate with 30 μm (b) and 40 μm (c)	61
5.8	(a) Table layout of the laser system for PC RF gun and (b) the photograph of the laser system	63
5.9	The schematic diagram of the synchronization between the laser and the master oscillator	64
5.10	The timing jitter is measured to be within an rms value of 126.5 fs by a phase detection method with Tektronix 11801B	66
5.11	Measured energy stability of the oscillator output is $< 1\%$ peak to peak	66
5.12	The optics layout of the THG, the UV stretcher, and the cross correlator (a) and the measured UV pulse length (b) with the home-made cross correlator	67
5.13	Quantum efficiency vs. different laser injection phase (a) and $\sqrt{\text{QE}}$ vs. $\sqrt{\sin\theta}$ (b). The measured quantum efficiency is 1.63×10^{-5} at a laser injection phase of 30° with minimum beam emittance by the beam dynamics simulation	71

LIST OF FIGURES

5.14	The laser injection phase vs. square root of the quantum efficiency about various electric field strengths at the cathode. The square root of the quantum efficiency peak is shifted along to the field strength	72
5.15	The electric field strength vs. the ratio between double peaks of the square root of the quantum efficiency. The peak ratio is linearly decreased along to increasing of the field strength	73
5.16	The position from the cathode vs. the beam energy about various laser injection phases at the electric field strength of 45 MV/m	73
5.17	Photoelectron charge vs. laser injection phase using the p- and the s-polarized lasers at a field of 45 MV/m on the cathode surface	74
5.18	The measured waveplate angle vs. the reflectivity of the laser (solid circle) and the waveplate angle vs. the quantum efficiency (empty circle)	75
5.19	(a) The electric field on the cathode vs the dark current. The dark current is squarely proportional to the electric field on the cathode. (b) The field enhancement factor by Fowler-Nordheim fitting is 120	78
5.20	The beam energy as a function of the laser injection phase with different field gradients	80
5.21	The beam energy as a function of the field gradient in the RF gun	81
5.22	The schematic diagram of the beam imaging system from the incident main beam to the beamlet. The beamlet is made by the single slit	84

LIST OF FIGURES

5.23	(a): Simulations (solid line) by the PARMELA code and experimental results (empty square) of the beam emittance evolution. The beam size evolution is represented a square dot on the graph. These data are measured under the conditions of the beam is 2.0 MeV beam energy and 0.35 nC beam charge. (b): The beam emittance and size evolution with 3.7 MeV beam energy and 0.3 nC beam charge	86
------	--	----

LIST OF TABLES

2.1	The design parameters of the PAL XFEL	8
2.2	The beam requirements of the Pohang Photo-Injector for the PAL XFEL..	11
4.1	Final tuned cavity microwave parameters under vacuum at temperature with 32.0 °C of the PC RF gun at PAL	44
5.1	Specifications of the laser for the PC RF gun	65
5.2	Achieved beam parameters from the PC RF gun at the GTS	85

CHAPTER 1

Introduction

1.1 Introduction

A high-charge and low-emittance electron beam is essential for the accelerator-driven facilities, e.g., the International Linear Collider (ILC) [1] and the fourth generation light sources such as the LCLS in USA [2], the European XFEL in Germany [1], the SCSS XFEL in Japan [3] and the proposed PAL X-ray Free Electron Laser (XFEL) at the Pohang Accelerator Laboratory [4-6]. In the past several years, we devoted most of our endeavors to design and to fabricate a photo-injector system [7, 8] which is intended for use in the femto-second electron diffraction (FED) facility [9-12] and the XFEL in PAL.

Chapter 1. Introduction

A high brightness electron beam [13-16] is conventionally provided by a photo-injector, where the beam is generated by ultra violet (UV) laser illuminating the cathode and is rapidly accelerated to the relativistic energy to reduce the emittance growth due to the space charge effect [17-19] as that occurs in a thermionic RF gun and a DC gun. The electron beam is further compressed by bunch compressors to provide high peak current to initiate self amplified spontaneous emission (SASE) instabilities that leads to efficient lasing in a single pass through the undulator [4, 20, 21]. The minimum wavelength of an XFEL scales in proportion to ε_n/γ , where ε_n is the normalized emittance and γ is the Lorentz factor. Thus, the most effective way to reduce the cost of an XFEL facility may be to produce low emittance and high-peak current electron beams rather than to increase the beam energy. The FED technique consists of the generation, measurement, and application of a variety of ultra-short beams. The photocathode (PC) RF gun at the PAL can generate ultra-short single electron bunch of the bunch length from 110 fs (FWHM) to 1 ps (FWHM) and sub-pC bunch charge for FED experiment.

In this thesis, we will concentrate on the following issues: the theoretical approach about the emittance compensation of the photo-cathode RF gun, the determination of the microwave parameters of the gun cavity, and various experimental results from the photo-cathode RF gun. The PAL XFEL and its photo-injector are introduced in Chapter 2. Chapter 3 describes the emittance definition, emittance compensation theory to minimize the emittance, and the computational approach of the emittance compensation. The microwave parameters of the gun cavity and the high power test of the microwave for the commissioning of the gun cavity are presented in Chapter 4. The various beam measurements, e.g. beam charge and energy scan about the laser injection phase, beam

Chapter 1. Introduction

emittance and size evolution along to the position from the cathode at the GTS are introduced in Chapter 5. Finally, Chapter 6 gives a conclusion and future works.

CHAPTER 2

Pohang Accelerator Laboratory X-ray Free Electron Laser and Its Pohang Photo Injector

2.1 Pohang Accelerator Laboratory X-ray Free Electron Laser (PAL XFEL)

The introduction of synchrotron radiation to Korean scientific community in 1994 by the construction of Pohang Light Source (PLS) was a memorial event in the Korean history of science. Since then Pohang Accelerator Laboratory (PAL) has successfully operated the PLS. Meantime, world light source community has seen a new and major advancement in the X-ray research area by X-ray Free Electron Laser (XFEL) based on Self-Amplified Spontaneous Emission (SASE). Light sources with an high peak

Chapter 2. Pohang Accelerator Laboratory X-ray Free Electron Laser and Its Pohang Photo Injector

brightness and a transverse coherence by the SASE will offer X-ray research scientists for the opening of new science [5, 6].

One of the key design issues is the beam energy. Current linac with 2.5 GeV beam energy should be extended and upgraded. Due to limitation of the space and the budget, the maximum beam energy is chosen to be from 3.5 to 4.0 GeV. However, X-ray users want to use the wavelength from 1.0 to 3.0 Å, which is difficult to achieve with this beam energy. The difficulty comes from the following two physical problems. First, the undulator radiation wavelength λ_r is given by

$$\lambda_r = \frac{\lambda_u}{2\gamma^2} (1 + a_u^2 + \gamma^2 \theta^2), \quad (1.1)$$

$$a_u = \frac{e \langle B_u^2 \rangle^{\frac{1}{2}} c \lambda_u}{2\pi m c^2}, \quad (1.2)$$

where λ_u is the undulator period, $\gamma m c^2$ is the beam energy, a_u is the undulator parameter, B_u is the undulator transverse magnetic field, $\langle B_u^2 \rangle^{\frac{1}{2}}$ is the rms over one undulator period, and θ is the angle of between the undulator axis and the direction at which the radiation is observed. Note, the relation between the frequently used undulator parameter K and a_u is $K = a_u \sqrt{2}$ for a planar undulator. If the radiation direction is on axis of the undulator, $\theta = 0$, Eq. (1.1) is given by

$$\lambda_r = \frac{\lambda_u}{2\gamma^2} \left(1 + \frac{K^2}{2} \right). \quad (1.3)$$

Using a conventional undulator with a period of a few cm, it is impossible to generate the radiation wavelength from 1.0 to 3.0 Å with the beam energy of less than 4.0 GeV.

Chapter 2. Pohang Accelerator Laboratory X-ray Free Electron Laser and Its Pohang Photo Injector

The second difficulty is related to the transverse coherence of the undulator radiation. In the SASE radiation, the transverse coherency is given by

$$\frac{\varepsilon_n}{\gamma} \sim \frac{\lambda_r}{4\pi}, \quad (1.4)$$

where ε_n is the normalized transverse emittance. Unless the PAL XFEL energy is higher enough, the SASE radiation can be achieved with relatively lower beam energy of the normalized transverse emittance is smaller than 1 mm-mrad. Thus, key issues of the PAL XFEL are the development of the in-vacuum undulator with higher undulator parameter and the development of the photo-injector with low transverse emittance. The design parameters of the PAL XFEL are summarized in Table 2.1. The PAL XFEL layout is shown in Fig. 2.1.

Chapter 2. Pohang Accelerator Laboratory X-ray Free Electron Laser and Its Pohang Photo Injector

Table 2.1: The design parameters of the PAL XFEL [6]

XFEL Beam Parameters (WFEL)	Value	Unit
Electron energy	3.7 (1.2)	GeV
Peak Current	3 (1.5)	kA
Normalized slice emittance	1	mm-mrad
RMS slice energy spread	0.01	%
Full bunch length	270	fs
Undulator parameters		
Undulator Period	1.5	cm
Segment length	4.5	M
Full undulator length	80	M
Peak undulator field	1.09	T
Undulator parameter, K	1.5	
Undulator gap	4	mm

Chapter 2. Pohang Accelerator Laboratory X-ray Free Electron Laser and Its Pohang Photo Injector

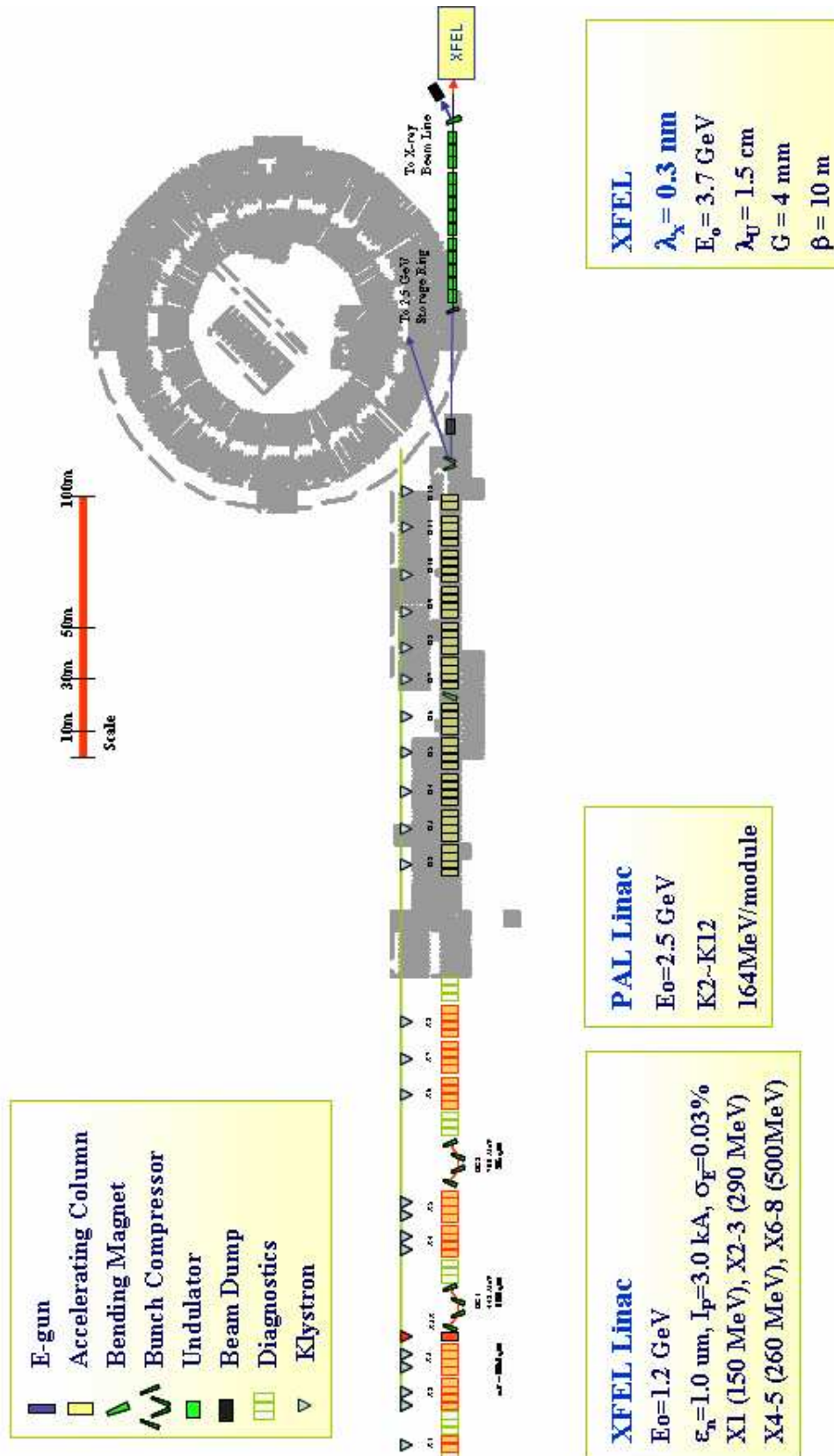


Figure 2.1: The design layout of the PAL XFEL.

2.2 The Pohang Photo-Injector (PPI) for the PAL XFEL

The PAL XFEL aims to achieve lasing at hard X-ray with relatively low beam energy (3.7 GeV) [4]. This fact inevitably requires very low emittance beams at the entrance of the undulator. If we assume the slice emittance requirement of < 1 mm-mrad (normalized, rms) at the undulator entrance, the injector of the PAL XFEL should provide the slice emittance better than 0.8 mm-mrad, with 25-% emittance increase during the transport through the driver linac. In terms of the usual projected emittance, this requirement would be translated into 1.0 mm mrad (normalized, rms).

The transverse emittance of the XFEL injector is not the whole story. It is generally known that the energy spread of the electron beam should be low for the efficient FEL interaction between the electron beam and the radiation, but not too much low in order to avoid the micro-bunching instability. Therefore, some means for controlling the energy spread of the electron beam should be provided, e.g., the laser heater as in the LCLS.

The injector for the PAL XFEL is required to produce a higher than 130-MeV with a single bunch of charge 1.0 nC with a normalized rms transverse emittance of 1.0 mm-mrad at a maximum repetition rate of 60 Hz. The requirements on the PPI for the PAL XFEL are quite challenging and necessitate careful designs and constructions of the injector for the PAL XFEL, the Pohang Photo-Injector (PPI) value to date lower than about 2 times.

In Table 2.2, we summarize beam requirements imposed on the PPI for the PAL XFEL. The schematic diagram of the PPI for the PAL XFEL is shown in Fig. 2.2. The photo-cathode RF gun for PAL XFEL, a thermionic gun for injection of the Pohang Light

Chapter 2. Pohang Accelerator Laboratory X-ray Free Electron Laser and Its Pohang Photo Injector

Source, and a polarized electron source (PES) gun are separately installed on the PPI site.

Table 2.2: The beam requirements of the Pohang Photo-Injector for the PAL XFEL

PPI Beam Parameters	Value	Unit	Note
Beam charge	1	nC	nominal
Beam energy	> 130	MeV	
Repetition rate	60	Hz	max.
Projected normalized transverse emittance	< 1.0	mm-mrad	rms
Un-correlated energy spread	$\sim 10^{-5}$		rms

Chapter 2. Pohang Accelerator Laboratory X-ray Free Electron Laser and Its Pohang Photo Injector

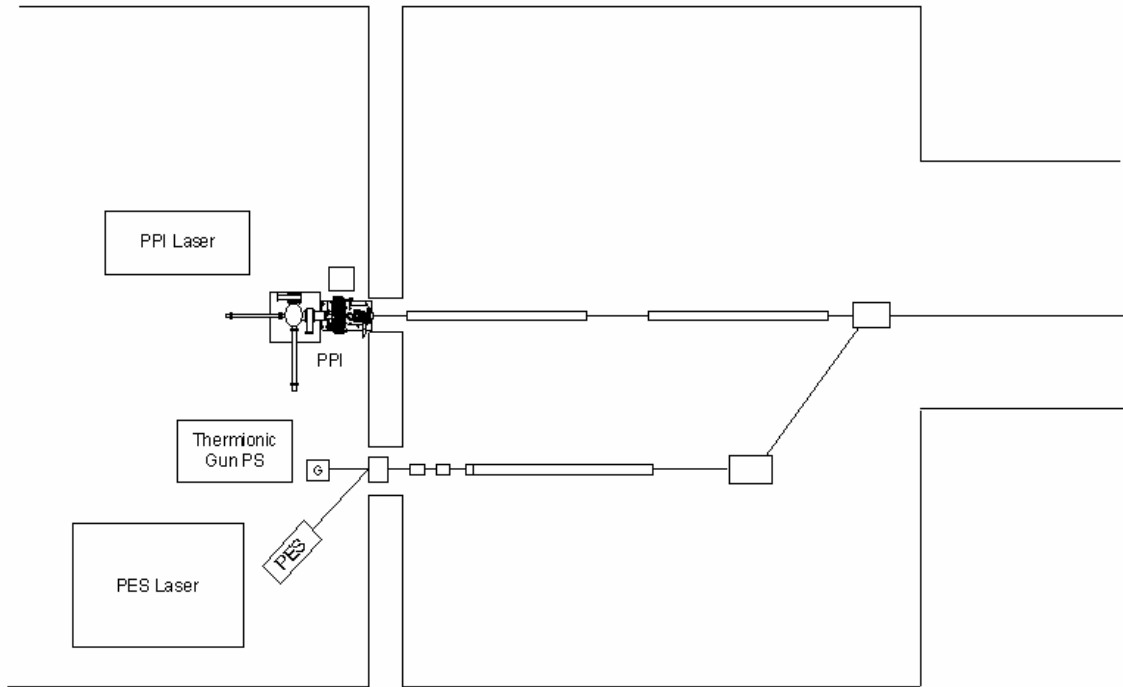


Figure 2.2: The schematic diagram of the PPI for the PAL XFEL. The photo-cathode RF gun for PAL XFEL, a thermionic gun for injection of the Pohang Light Source, and a polarized electron source (PES) gun are separately installed on the PPI site.

CHAPTER 3

Emittance Compensation Theory and Simulation

3.1 Introduction

The development of the photocathode radio-frequency gun in the last several decades [8, 13-16, 18] has made it possible to produce a high brightness electron sources to satisfy many advanced accelerator applications, such as a free electron laser [1-3, 5], linear colliders [1] and other applications [9-12]. A study of beam dynamics in the short-laser pulse driven radio frequency (RF) photocathode gun needs to take into account several effects, such as the dynamics due to the space-charge force and the dynamics due to the time variation of the RF acceleration force [17, 22-24]. Theoretical and

Chapter 3. Emittance Compensation Theory and Simulation

experimental approaches of these effects are essential to obtain injector with high-current, low-emittance, short bunch-length electron beams for the many advanced accelerator applications such as the free electron lasers (FEL) and international linear collider (ILC).

In the PARMELA simulation by proper conditions of RF gun and solenoid parameters, the emittance evolution shows an oscillation with a double minimum in the drift region due to the plasma oscillation of the laminar flow beam [17, 19]. According to Ferrario's new working point [17], the booster is located where the relative emittance maximum and the envelope waist occur, the second emittance minimum can be shifted to the booster exit and frozen at a very low value. It is studied by analytical, computational, and experimental approaches in the separated RF gun and the column to find the proper condition [13, 17, 22-24].

3.2 Emittance Definition

The definition of the geometrical rms emittance is given below with the unit of π mm-mrad [25-27]

$$\varepsilon_{rms} = \sqrt{\langle x^2 \rangle \langle x'^2 \rangle - \langle xx' \rangle^2}, \quad (3.1)$$

where each terms of Eq. (3.1) are defined as follows:

$$\langle x^2 \rangle = \frac{\iint x^2 \rho dx dx'}{\iint \rho dx dx'}, \quad (3.2)$$

$$\langle x'^2 \rangle = \frac{\iint x'^2 \rho dx dx'}{\iint \rho dx dx'}, \quad (3.3)$$

Chapter 3. Emittance Compensation Theory and Simulation

$$\langle xx' \rangle = \frac{\iint xx' \rho dx dx'}{\iint \rho dx dx'}. \quad (3.4)$$

The relation between the transverse geometrical and transverse normalized rms emittance is given by [28],

$$\varepsilon_{n,rms} = \beta\gamma\varepsilon_{rms}, \quad (3.5)$$

where $\beta = \frac{v}{c}$ and $\gamma = \frac{1}{\sqrt{1-\beta^2}}$ are the relativistic factors. Here, v is the velocity of

the electron and c is the speed of light. Figure 3.1 shows the transverse emittance on the transverse phase-space, where α , β , and γ are represented the Courant-Snyder parameters in the beam lattice, respectively [27, 29]. The projected emittance is always larger than the slice emittance because the projected normalized rms emittance is defined the integration along the longitudinal direction of the beam. Thus, the slice normalized rms emittance is defined by the integration for infinitesimal band of z and z' of the beam. The total normalized rms emittance of the electron beam is contributed by the each emittance terms, such as the emittance due to the space charge, ε_{sc} , the emittance due to the RF effects, ε_{rf} , and thermal emittance, ε_{th} [22]:

$$\varepsilon_{n,rms} \cong \sqrt{\varepsilon_{sc}^2 + \varepsilon_{rf}^2 + \varepsilon_{th}^2}. \quad (3.6)$$

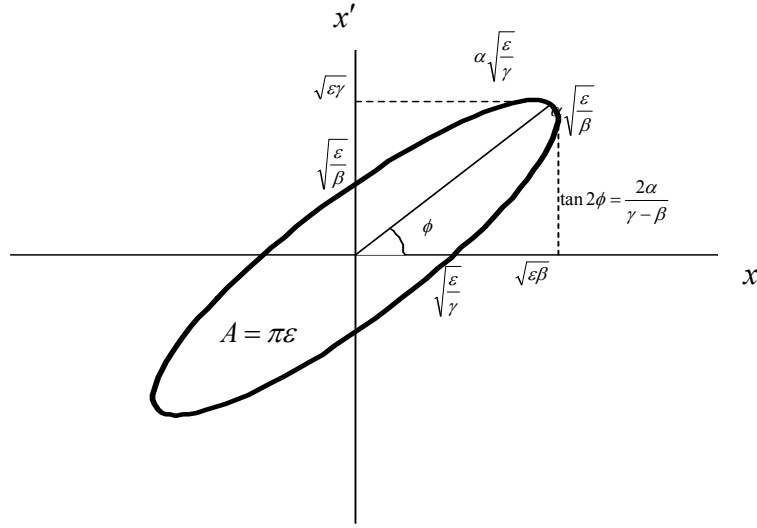


Figure 3.1: The phase space ellipse of the emittance

Thermal emittance due to the thermal energy of the photoelectron is defined as [30-32],

$$\varepsilon_{th} = \frac{\sigma}{2} \sqrt{\frac{E_{th}}{m_o c^2}}, \quad (3.7)$$

where σ is rms laser spot size on the cathode, $m_o c^2$ is the rest mass of the electron, and E_{th} is the thermal energy of the photoelectron. The thermal energy is determined by the difference of the work function of the cathode material (Φ) and the laser photon energy ($h\nu$) as given by,

$$E_{th} = h\nu - \Phi. \quad (3.8)$$

The space charge emittance, ε_{sc} , due to the repulsive force between electrons in the bunch causes the emittance to increase. The emittance due to the space charge effect is given by [22]

$$\varepsilon_{sc,(x,z)} = \frac{\pi}{4} \frac{1}{\alpha k} \frac{1}{\sin \phi_0} \frac{I_p}{I_A} \mu_{x,z}(A), \quad (3.9)$$

Chapter 3. Emittance Compensation Theory and Simulation

where $k = 2\pi/\lambda_{RF}$ is the wave number for the structure, ϕ_0 is the laser injection phase with respect to the RF, $I_A = 17\text{ kA}$ is the Alfvén current, and I_p is the peak current of the beam. The dimensionless strength parameter of the accelerating fields α is defined by

$$\alpha = \frac{eE_0}{2m_0c^2k}, \quad (3.10)$$

where E_0 is the peak accelerating field and e is the electron charge. The space charge factors for a longitudinal and a transverse Gaussian distribution beam, $\mu_{x,z}(A)$, are given by

$$\begin{aligned} \mu_x(A) &\approx \frac{1}{5+3A}, \\ \mu_z(A) &\approx \frac{1.1}{1+4.5A+2.9A^2}, \end{aligned} \quad (3.11)$$

respectively, where $A = \sigma_x/\sigma_z$ is the aspect ratio of the electron bunch that is defined the ratio between the transverse and the longitudinal rms beam spot sizes.

The RF emittance that results from a defocusing kick at the exit port is the effect due to the RF field in the RF gun. In 1.6 cell RF gun, the exit kick of the half cell is cancelled by the input kick of the full cell. The RF emittance of the transverse direction ($\varepsilon_{RF,x}$) and the longitudinal direction ($\varepsilon_{RF,z}$) are given by [14, 22]

$$\begin{aligned} \varepsilon_{RF,x} &= \frac{\alpha k^3 \sigma_x^2 \sigma_z^2}{\sqrt{2}}, \\ \varepsilon_{RF,z} &= \sqrt{3}(\gamma_f - 1)k^2 \sigma_z^3, \end{aligned} \quad (3.12)$$

respectively, where γ_f is the value of $\langle \gamma \rangle$ at the cavity exit. The phase-space distribution at the end of the $(n+1/2)$ th cavity is given by

$$\gamma = 1 + \alpha \left[(n + 1/2) \pi \sin \phi + \cos \phi \right]. \quad (3.13)$$

3.3 Theory of Emittance Compensation

An emittance compensation technique is used to reduce the rms beam emittance of the photo-injector for the free electron laser (FEL) [13, 18, 23]. The theory of linear emittance compensation has been by now understood that the optimization model of the photo-injector is the invariant envelop (IE). The emittance compensation technique has two basic ideas: The first idea is to use a solenoid to manipulate the transverse nonlinear space-charge force of the beam. The second one is to use booster linacs to freeze the beam transverse emittance from the beam of the space-charge dominated region to the beam of the emittance-dominated region by the RF acceleration force [17]. A study of beam dynamics in the photocathode RF gun driven by a short pulse laser needs to take into account several effects, such as the dynamics due to the space-charge force and the dynamics due to the time variation of the RF acceleration force [22].

In the RF acceleration process in the gun, the beams are accelerated from the rest at the photocathode emissive surface to relativistic energy at the exit of the gun cavity very quickly. The beams have a repulsive force due to large space-charge force by each electron in the bunch. The transverse phase space quality of the beams in the drift region is controlled and optimized by the externally applied focusing forces. In the rms envelop evolution equation, the normalized transverse emittance in the drift region is oscillated in a certain condition between the space-charge and the external focusing force. In these conditions, the beams go through plasma oscillations with the frequency due to the force between the emittance pressure and the external focusing.

Chapter 3. Emittance Compensation Theory and Simulation

If the accelerating structure exists in the drift region, the oscillation of the beam emittance is extended that the equation of the rms envelope evolution equation can be written as [23],

$$\sigma'' + \sigma' \left(\frac{\gamma'}{\beta^2 \gamma} \right) + K_r \sigma - \frac{\kappa_s}{\sigma \beta^3 \gamma^3} - \frac{\varepsilon_n^2}{\sigma^3 \beta^2 \gamma^2} = 0, \quad (3.14)$$

where σ is the rms beam size, γmc^2 is the mean beam energy, $\beta \equiv v_b / c = \sqrt{1 - \gamma^{-2}}$ is the normalized mean beam velocity, $K_r \equiv -F_r / r \beta^2 \gamma mc^2$ is strength of the external linear focusing channel, κ_s is the beam perveance, and ε_n is the normalized transverse emittance. It has been shown that the normalized transverse emittance oscillates with a frequency $\sqrt{2K_r}$ at an amplitude $\Delta \varepsilon_n \propto \sqrt{I_p / \gamma}$ whenever a bunched beam is matched into a focusing channel of gradient K_r [17, 23]:

$$\sigma_B(i) = \sqrt{\frac{I_p(i)}{2I_A (\beta \gamma)^3 K_r}}, \quad (3.15)$$

where σ_B is the rms beam size, $I_p(i)$ is the peak current at the i -th slice position, and $I_A = 17 \text{ kA}$ is the Alfvén current. Accelerating on the invariant envelope is given by

$$\sigma_i(i) = \frac{2}{\gamma'} \sqrt{\frac{I_p(i)}{3I_A \gamma}}, \quad (3.16)$$

where $\gamma' = eE_a / m_0 c^2 \approx 2E_a$, E_a is the accelerating field, which is a particular solution of the rms envelope equation in the laminar flow regime, leads to a damped oscillation of the emittance. The basic point in the design of the photo-injector is therefore to match the beam at injection into any accelerating section properly, according to the following conditions: A beam propagating through the structure on the invariant envelope will exit

Chapter 3. Emittance Compensation Theory and Simulation

the RF structure as a parallel beam that is given by

$$\sigma' = 0, \quad (3.17)$$

and the exit beam energy given as Eq. (3.16) with the accelerating field condition of

$$\gamma' = \frac{2}{\sigma} \sqrt{\frac{I_p}{3I_A \gamma}} \quad \text{for standing wave structure,} \quad (3.18)$$

$$\gamma' = \frac{2}{\sigma} \sqrt{\frac{I_p}{2I_A \gamma}} \quad \text{for traveling wave structure.} \quad (3.19)$$

These conditions give an rms match on the invariant envelope. Figure 3.2 shows the normalized rms transverse emittance, the rms beam spot size, and the beam energy evolution with a proper matching condition. The experimental approach to find the position of the parallel beam with the proper condition is essential to get the emittance compensated beam with minimum beam emittance.

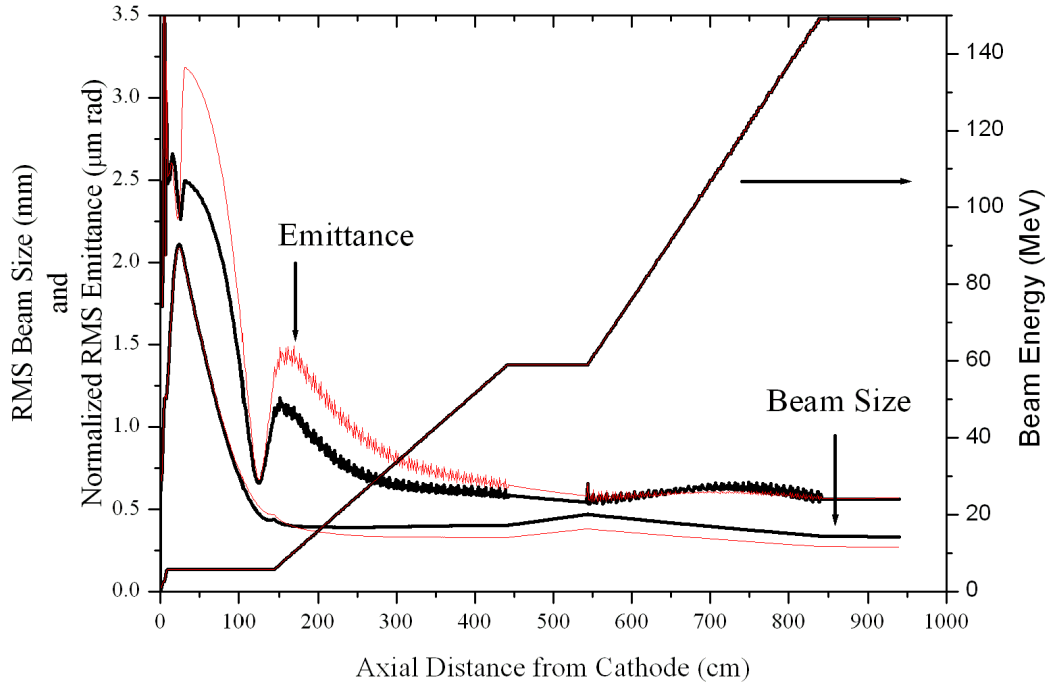


Figure 3.2: The emittance evolution simulation by the PARMELA code. The normalized rms transverse emittance at the simulation with the proper matching condition is damped to minimum value. The thick line is the LCLS photo-injector model and the thin line is modified our photo-injector model.

3.4 Simulation Study of the Photo-cathode RF Gun

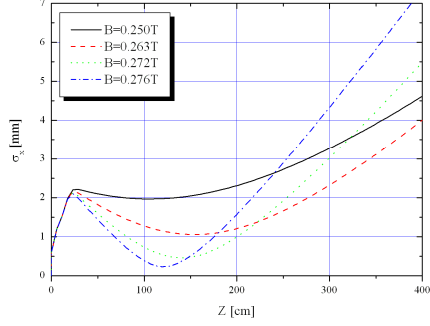
3.4.1 Simulation of the emittance evolution

Electromagnetic fields of the cavity are simulated by POSSION/SUPERFISH [33]. A resonant frequency of the 1.6 cell FR gun cavity is 2,856 MHz and the maximum electric field strength is 120 MV/m. But the experimental condition of our gun cavity is

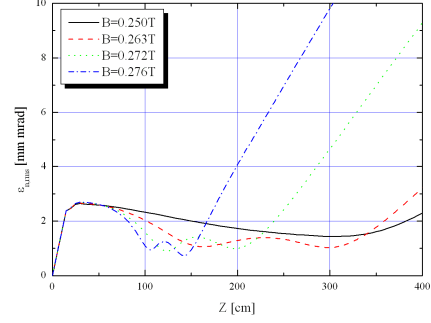
Chapter 3. Emittance Compensation Theory and Simulation

79 MV/m. The maximum magnetic field strength of the solenoid is 2.7 kG by Hall-probe, but the typical value during the experiment is 1.3 kG. The beam dynamics simulation about the beam size and the emittance evolution is carried out by the PARMELA code [34]. The electric field profile in the cavity and the magnetic field profile of the solenoid are shown Fig. 3.3 (a) and Fig. 3.3 (b), respectively. Figure 3.4 is shown the emittance and the beam spot size evolution about various electric fields with various magnetic fields.

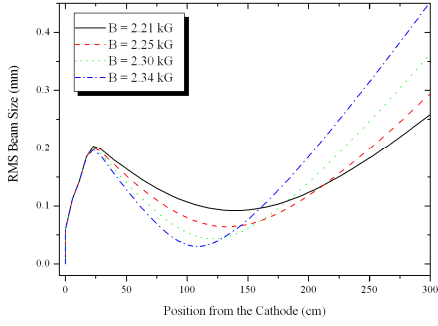
Chapter 3. Emittance Compensation Theory and Simulation



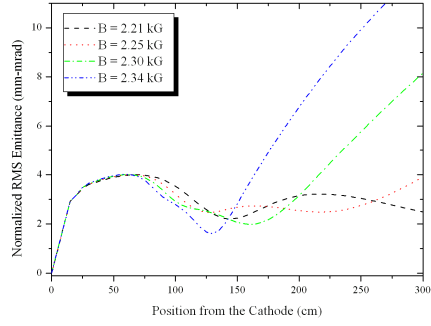
(a) $E_0 = 120$ MV/m



(b) $E_0 = 120$ MV/m



(a) $E_0 = 90$ MV/m



(b) $E_0 = 90$ MV/m

Figure 3.4: The evolution of the rms beam spot size (a), (c) and the emittance (b), (d) with various magnetic field strength of the solenoid. The simulations are performed with a 120 MV/m and 90 MV/m accelerating field gradient and a 1 nC and 0.4 nC beam charge, respectively.

3.4.2 Simulation of the beam dynamics in the cavity

The beam dynamics simulations in the cavity as a function of the laser injection phase are performed by the PARMELA code. The results of the simulations are represented the energy change in the cavity with 79 MV/m, 65 MV/m, and 53 MV/m electric field at the cathode as shown in Fig. 3.5, Fig. 3.6, and Fig. 3.7, respectively. In the low laser injection phase, the beam energy is increased in the both cells. However, in the high laser injection phase, the beam energy is increased and decreased at the end of the cells due to the deceleration forces. These phenomena are clearly appeared in the simulation with the low electric field at the cathode. Also, Fig. 3.8 shows the simulation results of the beam energy at the end of the cavity as a function of the laser injection phase with various electric fields in the cavity. The beam energy at the exit of the RF gun is decreased as the laser injection phase is increased with low electric field.

Chapter 3. Emittance Compensation Theory and Simulation

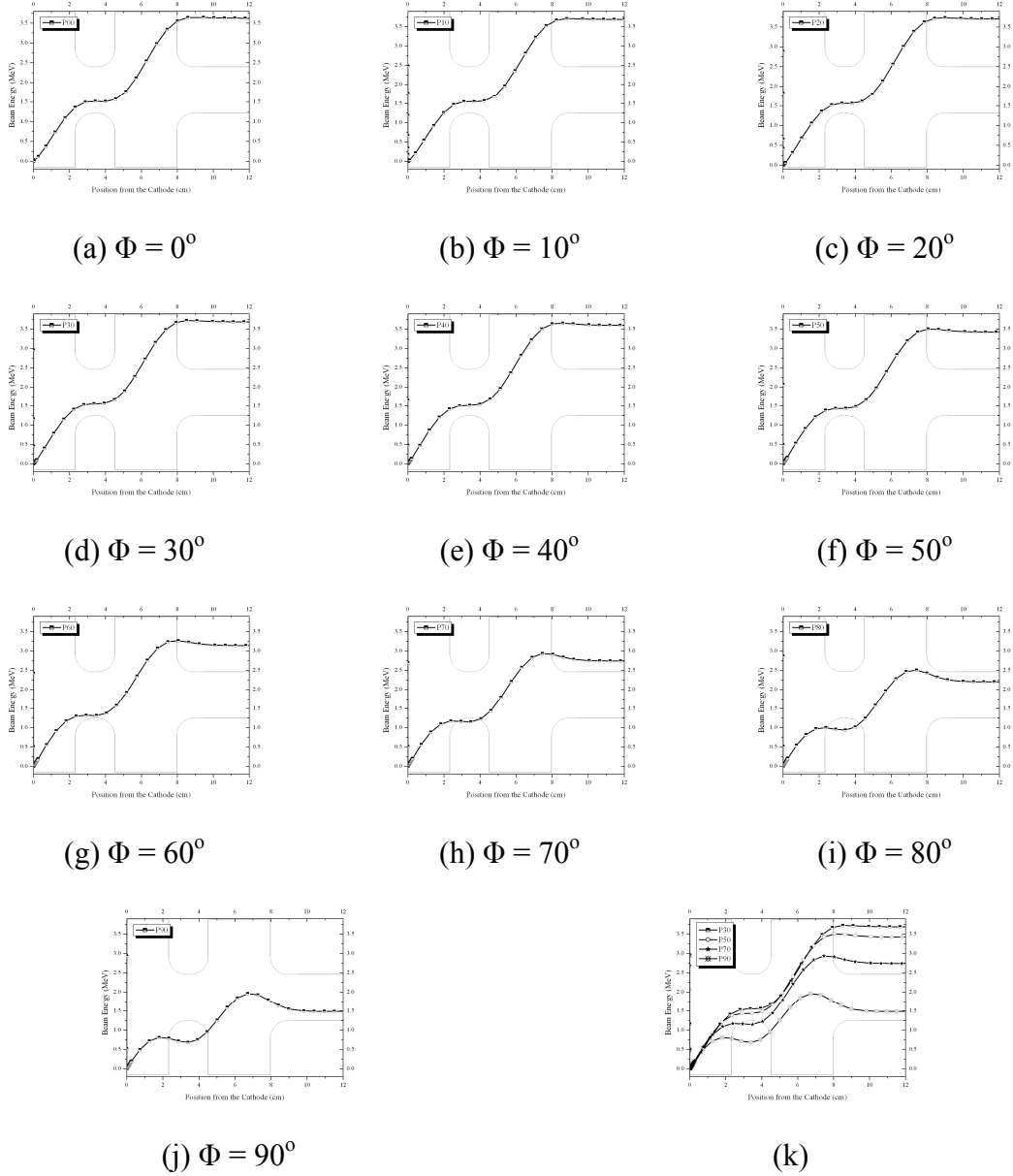


Figure 3.5: The beam energy simulation in the cavity as a function of the laser injection phase. These simulations are performed under the condition of a 79 MV/m electric field at the cathode.

Chapter 3. Emittance Compensation Theory and Simulation

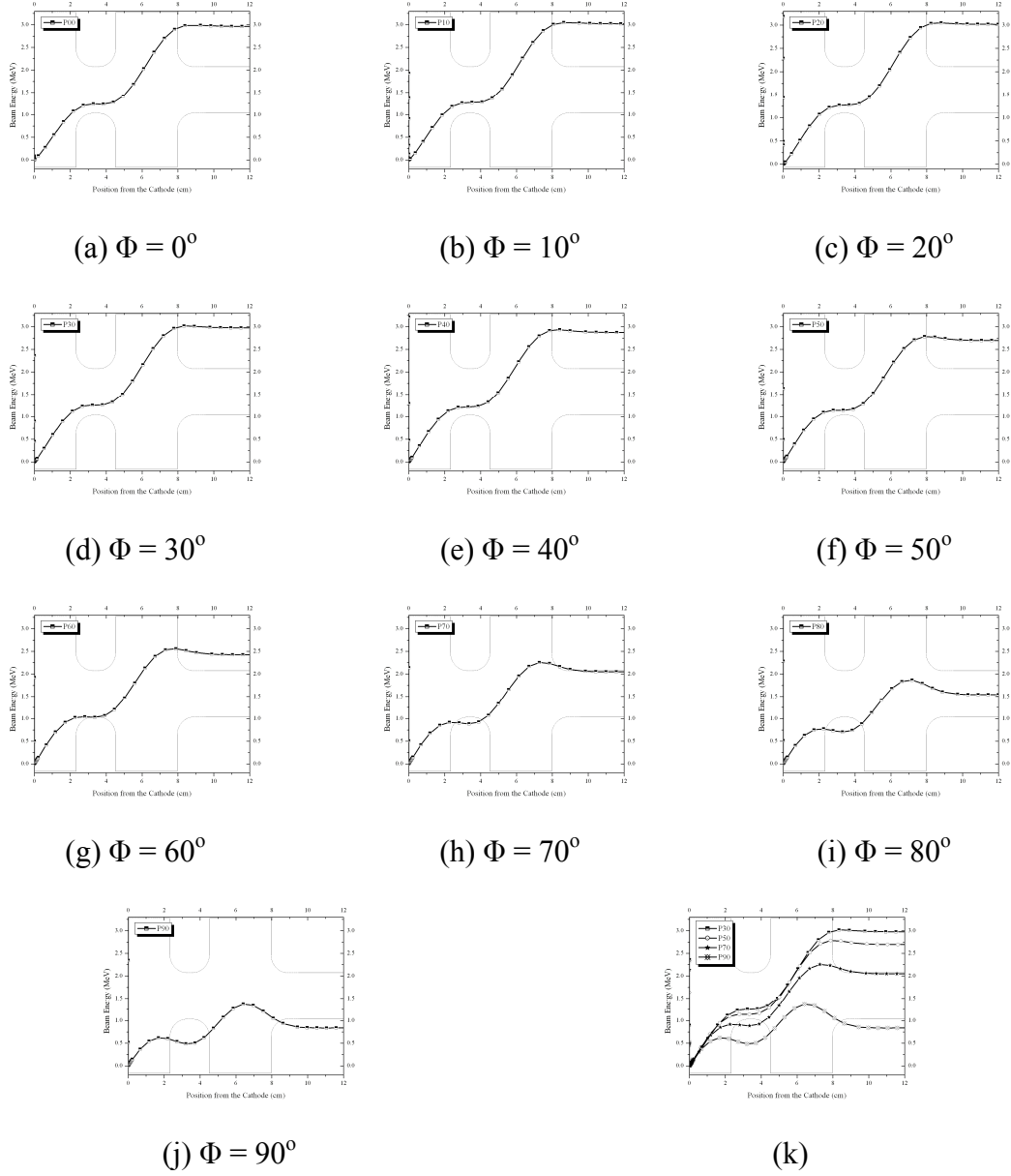


Figure 3.6: The beam energy simulation in the cavity as a function of the laser injection phase. These simulations are performed under the condition of a 65 MV/m electric field at the cathode.

Chapter 3. Emittance Compensation Theory and Simulation

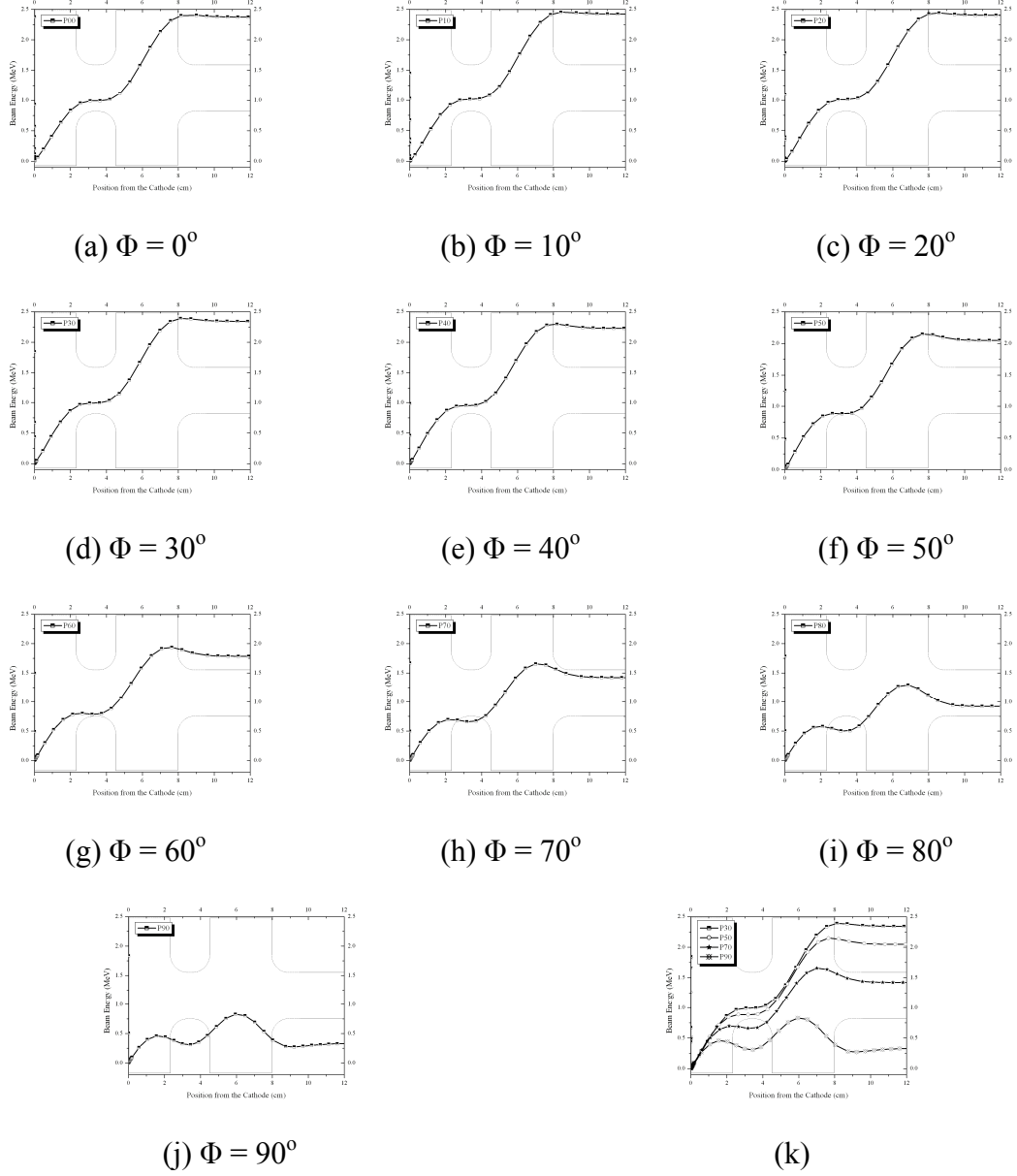


Figure 3.7: The beam energy simulation in the cavity as a function of the laser injection phase. These simulations are performed under the condition of a 53 MV/m electric field at the cathode.

Chapter 3. Emittance Compensation Theory and Simulation

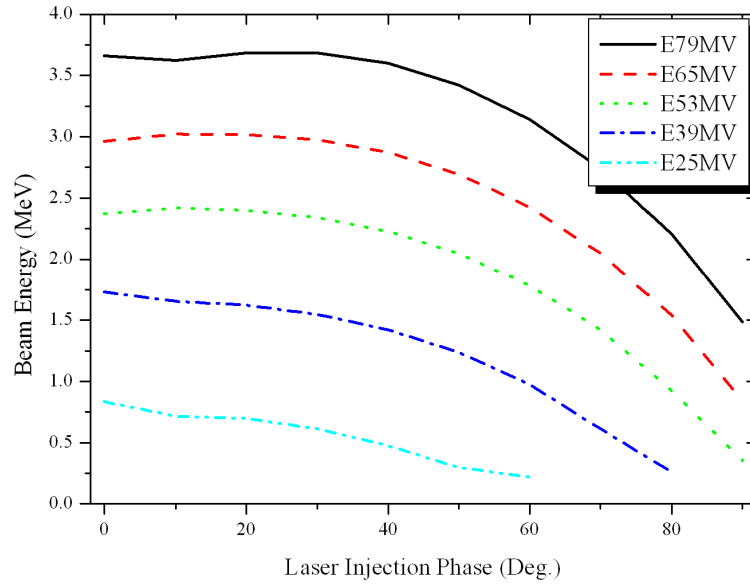


Figure 3.8: The beam energy simulation as a function of the laser injection phase with various electric fields in the cavity.

CHAPTER 4

RF Measurement and High Power Test

4.1 Cavity Design

4.1.1 Determination of the Cavity Diameter

The PC RF gun was developed and fabricated by collaboration of the Brookhaven National Laboratory (BNL), the Korea Advanced Institute of Science and Technology (KAIST), and the PAL. The laser-driven copper-cathode 1.6-cell RF gun cavity consists of a half-cell and a full-cell. The half cell of the 1.6-cell cavity is symmetrized by two laser ports which are angled 45° from the waveguide port. Tuners, a pumping port, and a waveguide port are placed in the full cell. The laser incident port makes an angle of

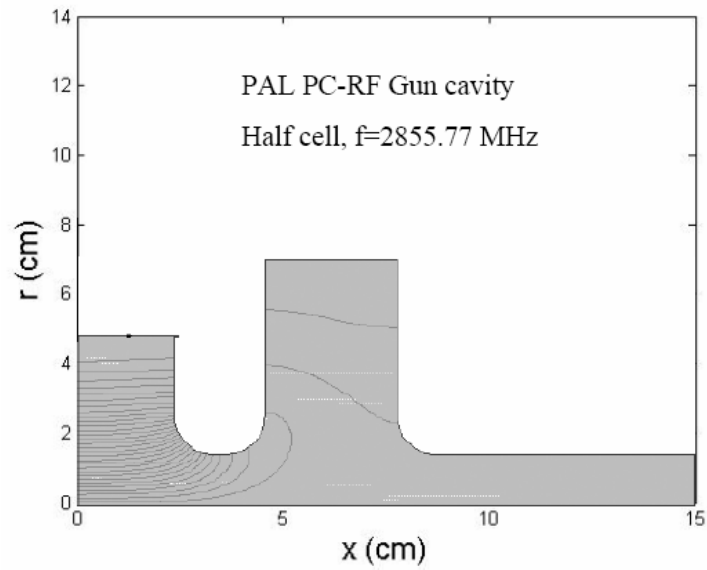
Chapter 4. RF Measurement and High Power Test

67.5° between the laser propagation direction and the cathode surface, allowing for UV laser to flash the cathode surface and to minimize the transmission loss. The gun is operated in π -mode at 2,856 MHz RF frequency with multipole suppression achieved through the cavity symmetrization. The coupling between the waveguide and the full cell is accomplished via the coupling slot on the full cell cavity. RF power from the full cell couples to half cell through the iris by electric coupling. In order to reduce the space-charge induced emittance growth, the photoelectrons should be quickly accelerated in the gun.

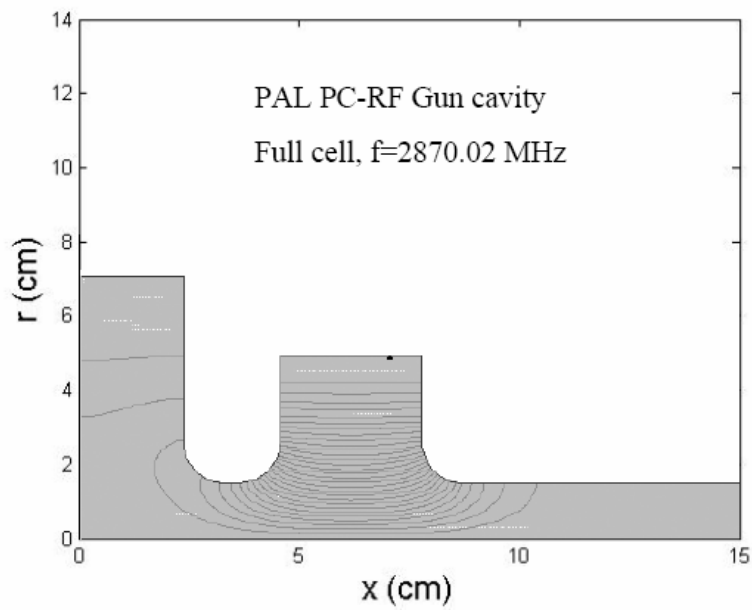
The cavity dimension that provides the desired resonant frequency can be determined with a 2D numerical code SUPERFISH [33] which calculate the resonant frequency for each cell without taking account of the laser port and the waveguide port. The resonant frequency for each cell can be written as [35] ,

$$\begin{aligned} f_1 &= f_\pi \left(1 - \frac{k\sqrt{r}}{2} \right), \\ f_2 &= f_\pi \left(1 - \frac{k}{2\sqrt{r}} \right), \end{aligned} \quad (4.1)$$

where f_1 and f_2 are resonant frequency of the half and the full cells, respectively, f_π is the required π -mode frequency, k is the coupling factor between two cells, and $r = 1.67$ is the volume ratio of the full cell to the half cell. The f_1 and f_2 are found to be 2,853.861 MHz and 2,854.717 MHz, respectively, using the designed value $k = 1.16 \times 10^{-3}$ and $f_\pi = 2,856$ MHz. The rough dimensions of each cell of the 1.6-cell cavity are determined by SUPERFISH code while making the other cell completely detuned, and the results are shown in Fig. 4.1. After the dimensions are determined, two cells are combined to yield the 0-mode and the π -mode at the required frequency.



(a)



(b)

Figure 4.1: Simulation with SUPERFISH 2D code to determine resonant frequencies:

(a) Half cell, 2,855.77 MHz; (b) full cell, 2,870.02 MHz.

Chapter 4. RF Measurement and High Power Test

Directions of the electric field in each cell are the same at 0-mode while they are opposite to each other at π -mode as shown in Fig 4.2. With π -mode resonant at 2,856.0 MHz, the mode separation between the 0-mode and the π -mode is 3.4 MHz which provides a good field balance that is crucial for the generation of low emittance electron beam.

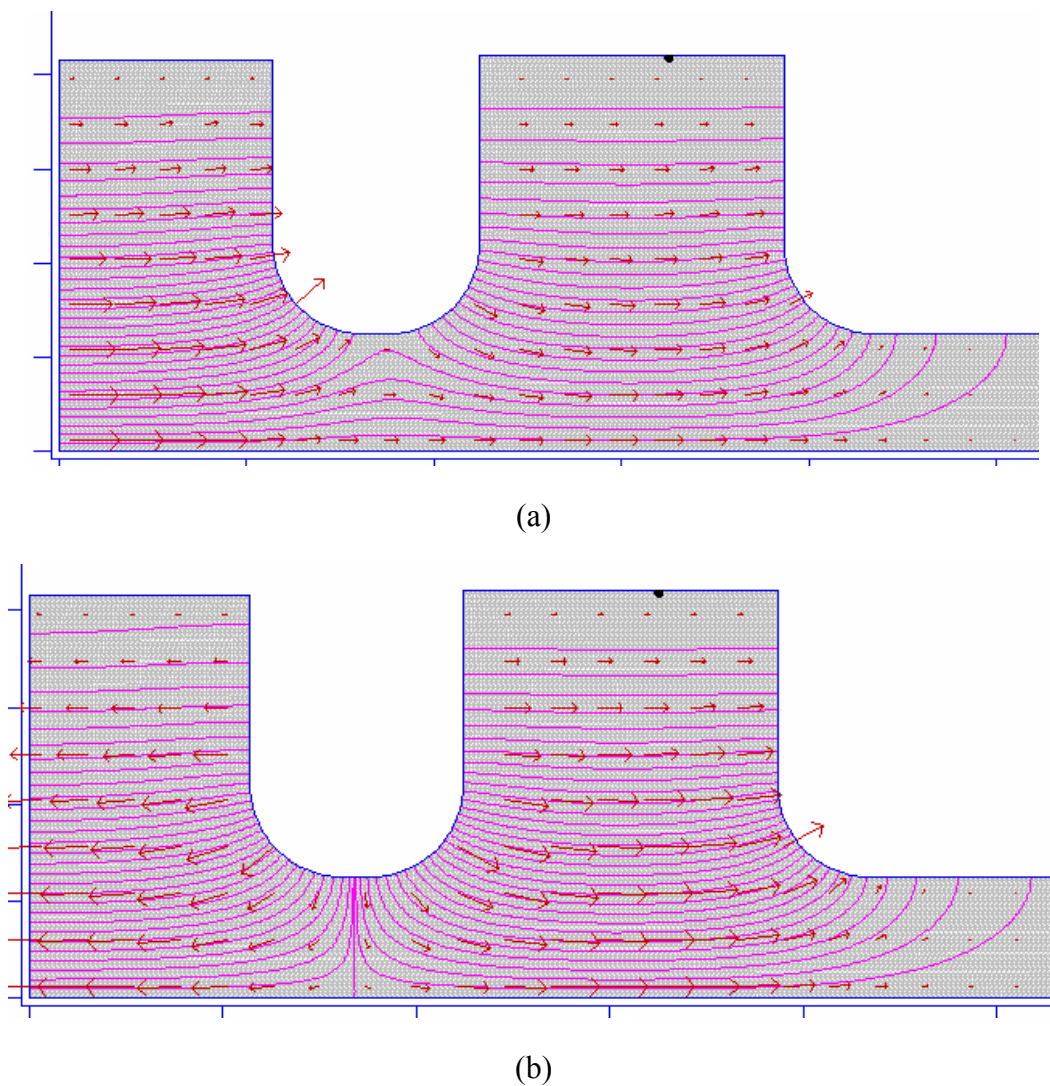


Figure 4.2: Electric field drawing in the cavity at the 0-mode (a) and the π -mode (b) using the SUPERFISH simulation.

Chapter 4. RF Measurement and High Power Test

When a laser port and a waveguide port are introduced, the resonant frequency changes. Note this cannot be handled with SUPERFISH code. 3D codes such as MAFIA [36] and HFSS [37] can only provide the resonant frequency with an accuracy of about 1 % that cannot fulfill the requirement of the cavity. However, the change of the resonant frequency due to the presence of the laser and the waveguide ports can be calculated as accurate as 0.1 MHz by Slater's perturbation theorem [28]. Thus, we will estimate the frequency variation with Slater's perturbation theorem. This tuning process to determine the specific size for two ports, that will provide the designed resonant frequency exactly, is conducted under the guidance of perturbation formula that can handle the frequency variation due to 3D effects. According to the perturbation theorem, if the perturbation occurred in a small volume as compared to the whole cavity, the frequency variation $\delta\omega(= \omega - \omega_0)$ can be calculated as [38, 39],

$$\delta\omega = \frac{\omega_0}{4U} \int_{\Delta v} (\mu_0 H^2 - \epsilon_0 E^2) dv, \quad (4.2)$$

where ω_0 is the unperturbed resonant frequency, ω is the perturbed frequency, U is the stored energy in the cavity, and H and E are the magnetic and the electric field in the small volume, respectively. When the perturbation is exerted on the cavity wall, the frequency change due to the cavity wall volume variation can be expressed as [38, 39],

$$\omega^2 = \omega_0^2 \left(1 - \frac{2\Delta U_m}{U} (1 - e^{-2\alpha z}) \right), \quad (4.3)$$

where ΔU_m is the time-averaged magnetic energy stored in the perturbation volume, α is the attenuation factor, and z is the thickness of the cavity wall.

There is still one thing we would like to point out that the perturbation formula alone is not sufficient to predict exact dimensions of the cavity fully. Thus, we repeated the cutting of the inner diameter of the cavity and then measuring of the resonant frequency of the cavity by the network analyzer, so called the cutting and measuring process, until the desired resonant frequency is achieved.

4.1.2 Modification of Coupling Coefficient

The microwave parameters are measured by HP 3510C Network Analyzer under the standard temperature, pressure, and humidity (STPH) condition. Coupling coefficient at the π -mode is different from the final tuned goal of 1.00. The coupling coefficient is under-coupled with 0.35 where the resonant frequency of π -mode is measured to be 2,855.7 MHz and the mode separation is 3.4 MHz. In order to increase the coupling coefficient to the desired value, Bethe's theory of small aperture coupling is used for the tuning of the coupling coefficient. The coupling coefficient behaves as [38-40] ,

$$\beta_{rf} = \frac{\pi^2 Z_0 k_0 \Gamma_{10} e_0^4 l_1^6 e^{-2\alpha_0 d}}{9 a b [K(e_0) - E(e_0)]^2} \frac{H_1^2}{P_0}, \quad (4.4)$$

where Z_0 is the impedance of free space, k_0 is the wave number in the free space, l_1 is the coupling slot size, d is the coupling slot thickness, H_1 is the magnetic field strength on the wall of the cavity, and P_0 is the total power loss in the cavity. For a cylindrically symmetric cavity, H_1^2/P_0 can be calculated with SUPERFISH code. We also repeated the cutting and measuring process about the coupling slot until the desired coupling coefficient is achieved. With the finalized coupling slot size, the coupling

coefficient is measured to be 1.26 which is slightly over-coupled and the resonant frequency of π -mode is 2,855.7 MHz.

4.1.3 Beam Dynamics Simulation

Focusing solenoids with 8-pancake coils are designed by POISSON code [33]. The designed field map produced by POISSON code provides a good emittance compensation when the excitation current is about 180 A, as shown in Fig. 4.3 (a), (b). The field measurement for a focusing solenoid has been performed. The designed electric field in the cavity is used by SUPERFISH for PARMELA simulation [34]. The field profile from the PARMELA simulation is given as shown in Fig 4.3 (c). The field map is further used in the simulation of beam dynamics with PARMELA code. From these, simulation results for the emittance evolution, the beam size evolution, and the energy evolution are shown in Fig. 4.3 (d). The simulation with the designed field profile indicates that the PC RF gun in the PAL is capable of producing low emittance electron beam. To perform the desired emittance compensation, the uniformity of the magnetic field of the solenoid is very important. The maximum solenoid current is 200 A and the maximum field strength is 2,985.8 Gauss. The uniformity of the axial magnetic field at the center of the solenoid is better than 10^{-4} . The offset between the mechanical center and the field center of the solenoid is found to be less than 0.1 mm, which is acceptable.

Chapter 4. RF Measurement and High Power Test

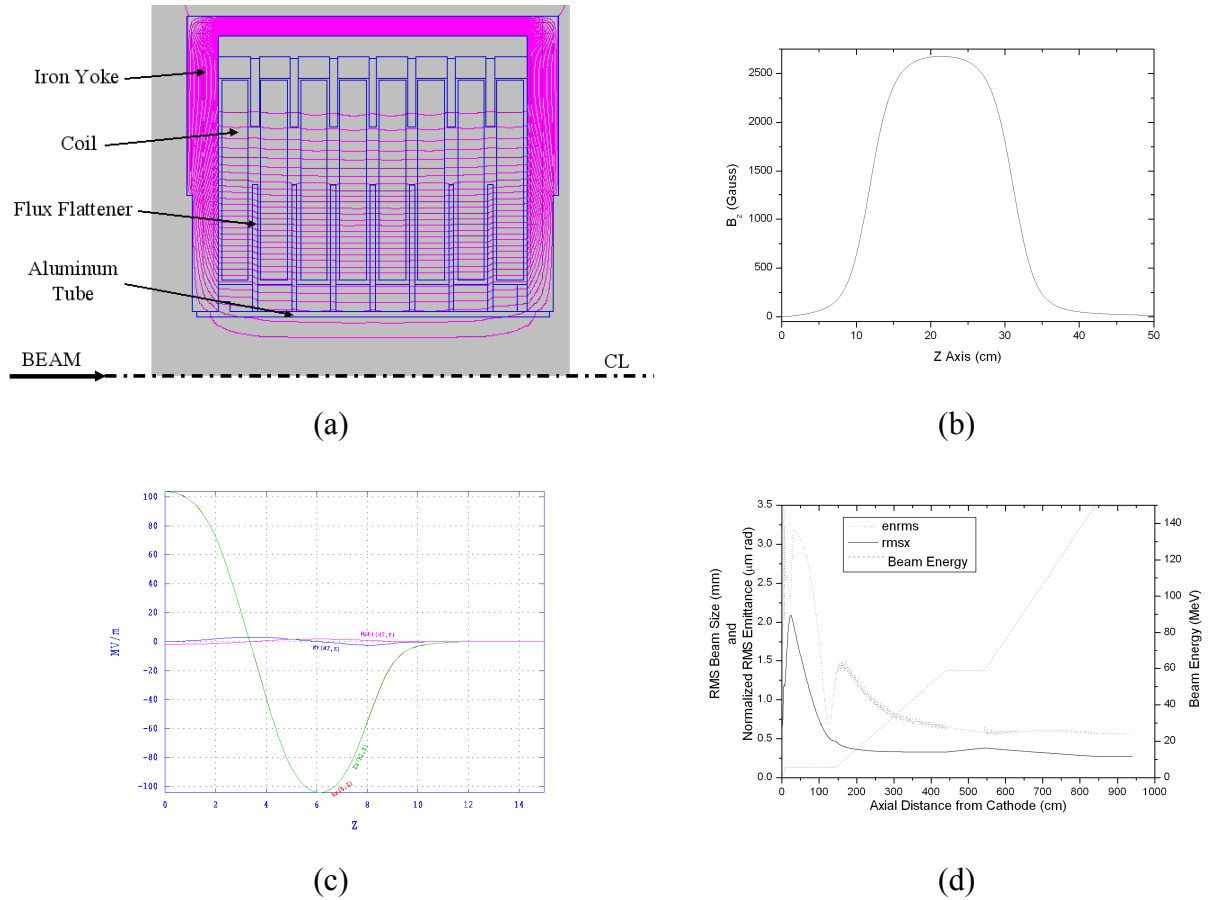


Figure 4.3: (a) The designed field profile of the solenoids with POSSION code, (b) the measured field profile with the field measurement device, (c) the designed electric field in the cavity, and (d) the simulation results for the normalized emittance evolution (dotted line), the beam size evolution (solid line), and the beam energy evolution (dashed line).

4.2 Microwave Characterizations

4.2.1 Measurement with the Model Cavity

Before embarking in the fabrication of the RF gun, we have prepared a cold model to check the tuning property of the gun cavities. Figure 4.4 shows the model cavity that has two tuners and loop couplers installed at each cell, which allow easy checks of cavity tuning properties.

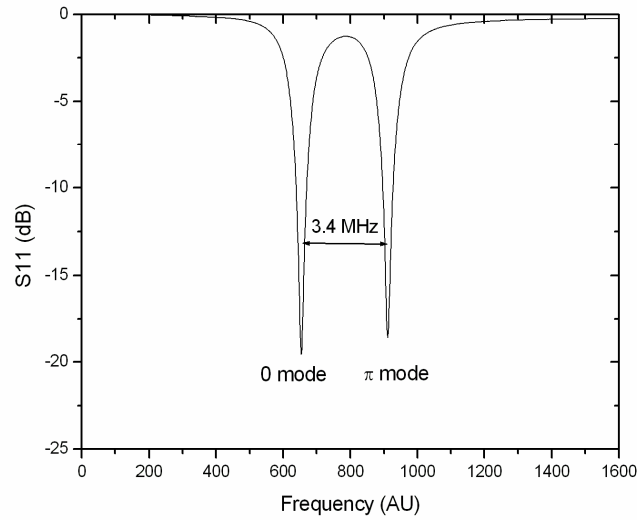


Figure 4.4: The photograph of the model cavity to check the tuning property of the gun cavity.

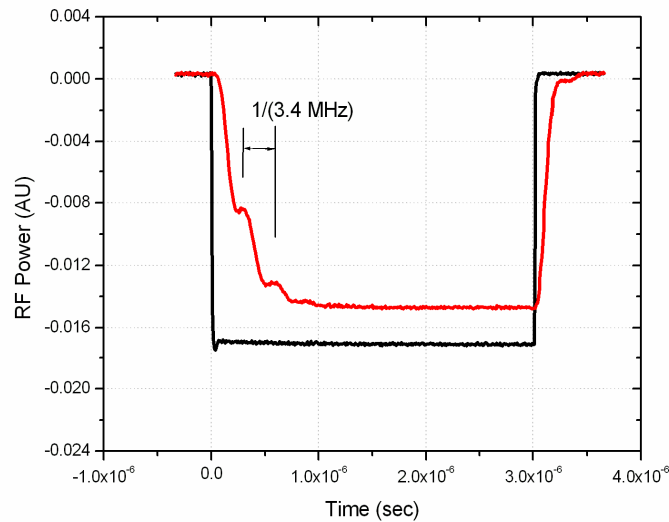
Chapter 4. RF Measurement and High Power Test

Network-analyzer measurement of the two resonant modes in the gun cavity is shown in Fig. 4.5 (a). With the π -mode resonance at the 2856 MHz, the mode separation between the 0- and the π -mode was 3.4 MHz. The suppression of the 0-mode is not done because the loop coupler used in this cold model is wide-band. Transient response of the gun cavity to pulsed RF power is important because of the mode beating phenomenon. By applying pulsed RF to the full-cell coupler, the time evolution of cavity field is observed at the other coupler in the half cell. Figure 4.5 (b) is shown the time-profile of the cavity field together with the input RF waveform of the square line. The rippling in the rising part of the cavity-field waveform is believed to be caused by the mode beating. Note the period of the rippling corresponds to the inverse of the mode separation. Since the characteristic time of the standing-wave cavity is proportional to the Q-factor of the cavity, measured transient period shown in Fig. 4.5 (b) is different from the real gun that is made of brazed copper. Also notice that the falling part of the cavity-field waveform is a simple exponential decay, which would be the indication of the enough decay of the 0-mode during the RF pulse. The relevance of these observations to the practical aspect of the gun operation is that the pulse duration of the rf power input should be long enough to allow the 0-mode to decay sufficiently. Otherwise, the condition of the cell balance is not met and the beam quality is deteriorated.

The resonant frequency change as function of the tuner depth on the cavity wall surface is shown in Fig. 4.6. Its relation is non-linear because different frequency effects are given by the magnetic field properties at different positions from the cavity wall surface.



(a)



(b)

Figure 4.5: (a) Network-analyzer measurement of the two resonant modes in the gun cavity and (b) transient response of the gun cavity to pulsed RF power. The mode separation is measured to be 3.4 MHz.

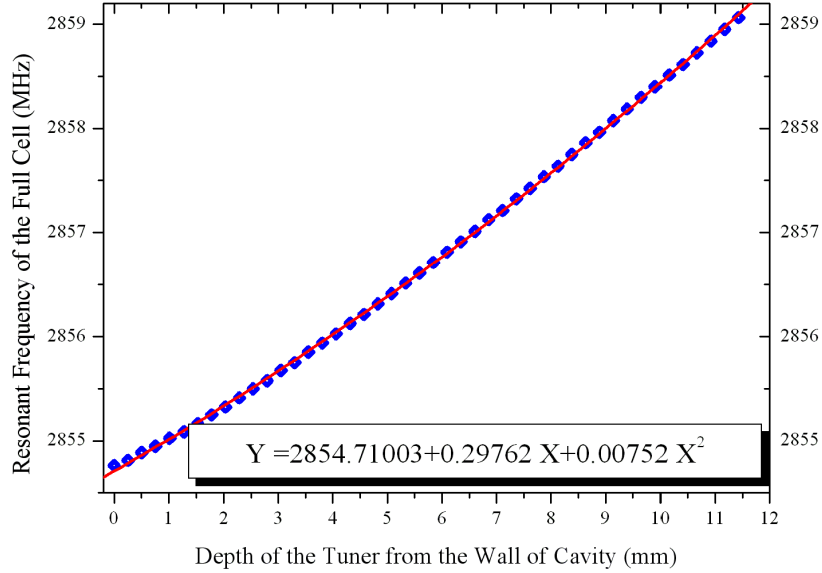


Figure 4.6: The resonant frequency change as a function of the tuner depth on the cavity wall surface. Its relation is non-linear because different frequency effects are given by the magnetic field properties at different positions from the cavity wall surface.

4.2.2 Measurement of the Cavity

The RF gun cavity is finally brazed with the waveguide for transmission of the RF power from the RF system. Vacuum components such as an RF window for power transmission, an ultraviolet window for laser beam incidence, a gate valve, and a tuner for frequency tuning under vacuum state are assembled. There is a 1 MHz increase in the resonant frequency when the cavity is in vacuum state as compared to that in air, so we further tuned the resonant frequency to 2,855.25 MHz by adjusting the position of the cathode plate with a push-and-pull screw as well as by using the cavity tuner.

The microwave parameters are measured and the results are shown in Fig. 4.7. From the S_{11} parameter in Fig. 4.7 (a), we see that the resonant frequency of π -mode is

Chapter 4. RF Measurement and High Power Test

2,856.25 MHz with a mode separation of 3.4 MHz under vacuum state at room temperature (25 °C). An unloaded quality factor (Q_0) is calculated from Fig. 4.7 (b). An unloaded half-power point (UHPP) can be written as [40-42]

$$\beta_{3,4} = \frac{2 + \beta^2 + \sqrt{4 + \beta^4}}{2\beta}, \quad (4.5)$$

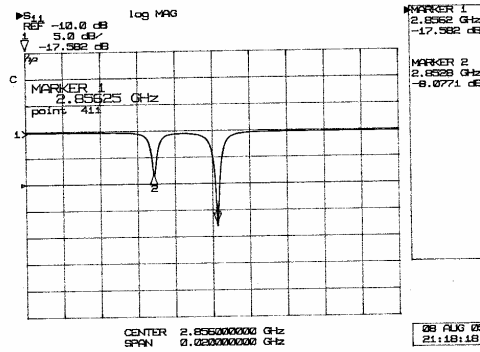
where $\beta = 1.26$ is the coupling coefficient, and $\beta_{3,4}$ is calculated to be 2.45 from Eq. (4.5). The frequency of the UHPP is measured to be 2,856.1 MHz and 2,856.4 MHz at each side of the resonance as shown Fig. 4.7 (b). Figure 4.7 (b) is the voltage standing wave ratio (VSWR) chart that shows the coupling coefficient is about 1.26. The unloaded quality factor can be obtained from the resonant frequency divided by the frequency difference of the UHPP and is found to be about 9,000. Figure 4.7 (c) is the impedance circle from which we see that the cavity is over-coupled. To guarantee a good operation and to tune the resonant frequency to the exact designed value, a precision cooling system is installed to maintain the mechanical dimensions of the PC RF gun. The measured resonant frequencies by the HP 3510C network analyzer with different temperature conditions of the cavity are 2,856.25 MHz at 25.0 °C and 2,856.0 MHz at 32.0 °C, respectively. Figure 4.8 shows the measured frequency with different temperature of 3.4 MHz mode separation. The frequency shift as a function of temperature variation is measured and shown in Fig. 4.9. The linear fitting indicates that the resonant frequency will be decreased by 42.37 kHz if the temperature increases by 1 °C and vice versa. After increasing the temperature from 25 °C to 32 °C, the desired resonant frequency of 2,856.00 MHz is achieved. The RF parameters under the vacuum state at the cooling temperature with 32 °C are summarized in Table 4.1.

Chapter 4. RF Measurement and High Power Test

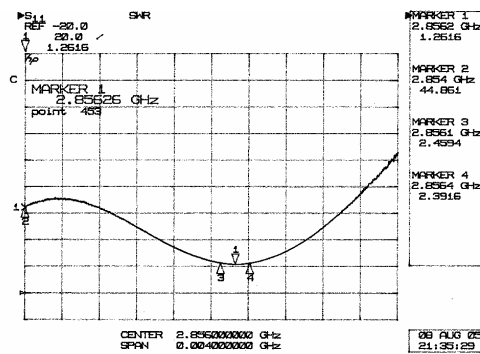
Table 4.1: Final tuned cavity microwave parameters under vacuum at temperature with 32.0 °C of the PC RF gun at PAL

Parameter	Values	Unit
π -Mode	2856.0	MHz
0-Mode	2852.6	MHz
RF Pulse Width	2.0	μs
Coupling Coefficient	1.26	-
Quality Factor	9000	-
Cathode Type	Copper	
Work Function of the Cathode	4.65	eV
Photon Energy at UV	4.67	eV

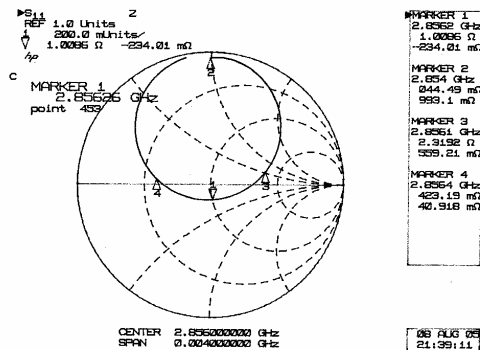
Chapter 4. RF Measurement and High Power Test



(a)



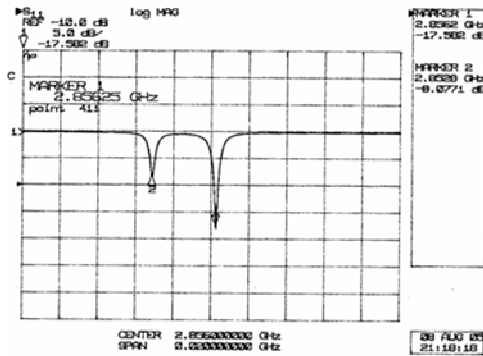
(b)



(c)

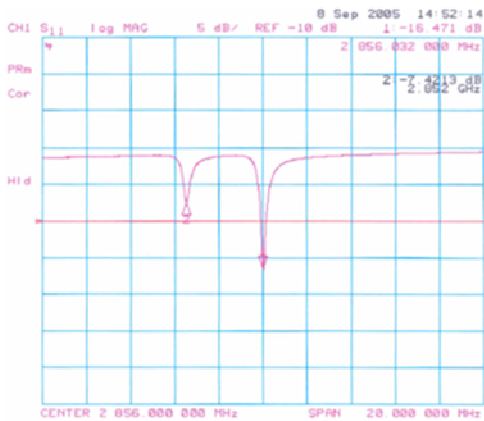
Figure 4.7: The measured microwave parameters: (a) the measured S_{11} parameter, (b) the measured VSWR chart, and (c) Smith chart under the vacuum at room temperature (25 °C).

Chapter 4. RF Measurement and High Power Test



S₁₁ Measurement

- $f_{\pi} = 2856.25 \text{ MHz @ } 25 \text{ }^{\circ}\text{C}$
with vacuum inside the cavity
- Mode Separation = 3.4 MHz



S₁₁ Measurement

- $f_{\pi} = 2856.00 \text{ MHz @ } 32 \text{ }^{\circ}\text{C}$
with vacuum inside the cavity
- Mode Separation = 3.4 MHz

Figure 4.8: The S₁₁ measurement of the cavity under vacuum condition at the different temperature by the network analyzer: In the upper figure, the π -mode resonant frequency at the 25.0 °C is 2,856.25 MHz with 3.4 MHz mode separation. In the bottom figure, the π -mode resonant frequency at the 32.0 °C is 2,856.0 MHz with the same mode separation.

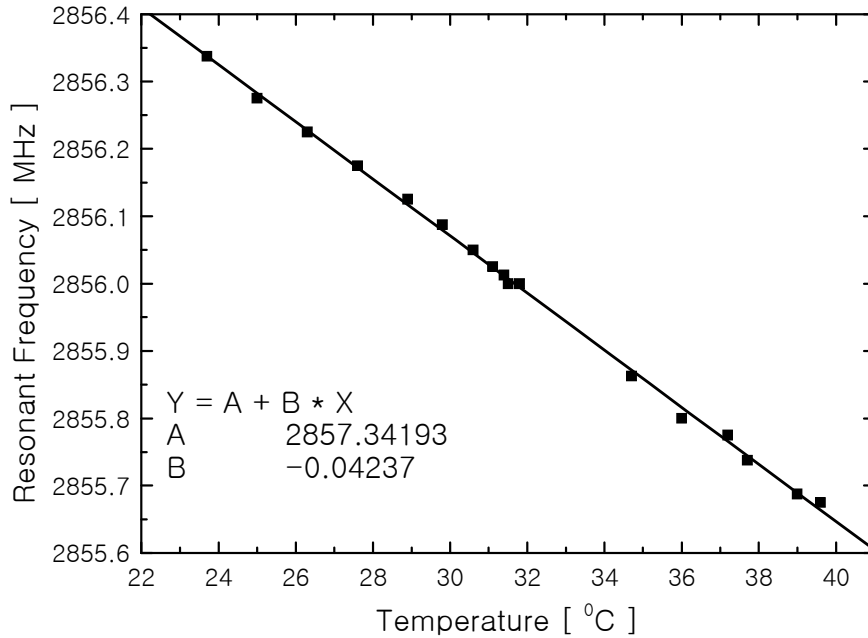


Figure 4.9: The measured resonant frequency as a function of the temperature in the cavity. The temperature coefficient is measured $-42.37 \text{ kHz}/^\circ\text{C}$.

The gun cavity is finally installed at the site with a directional coupler between the klystron and the gun cavity as shown in Fig. 4.10. In order to guarantee a good operation of the PC RF gun, a method to measure the resonant frequency during the gun operation is developed. The method uses a 2,856 MHz klystron which has a 3-dB bandwidth of about $\pm 5 \text{ MHz}$ [43] and a directional coupler in the klystron waveguide. The resonant frequency is obtained via the measurement of the ratio of forward to reflected power when the cavity cooling temperature is maintained at $32.0 \text{ }^\circ\text{C}$ with the precision cooling system and the results are shown in Fig. 4.11. The forward and the reflected powers are measured by a calibrated crystal detector. The resonant frequency

Chapter 4. RF Measurement and High Power Test

of π -mode is 2,856.1 MHz with 3.46 MHz of the mode separation. Its measurement is performed with 0.2 MHz frequency step.

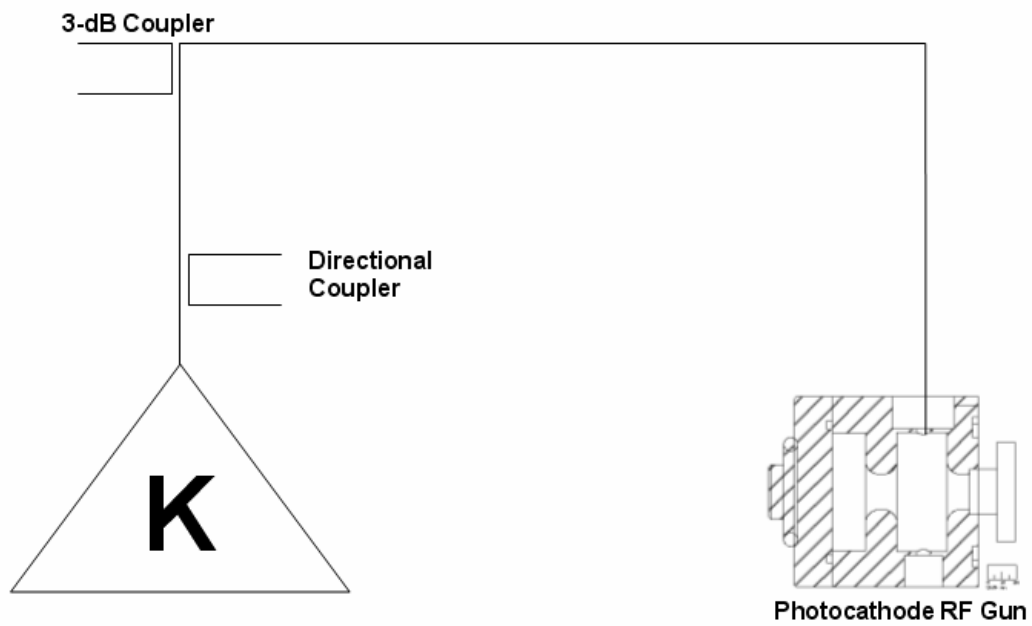


Figure 4.10: Schematic diagram of the RF network of the photocathode RF gun. Symbol

K means a klystron.

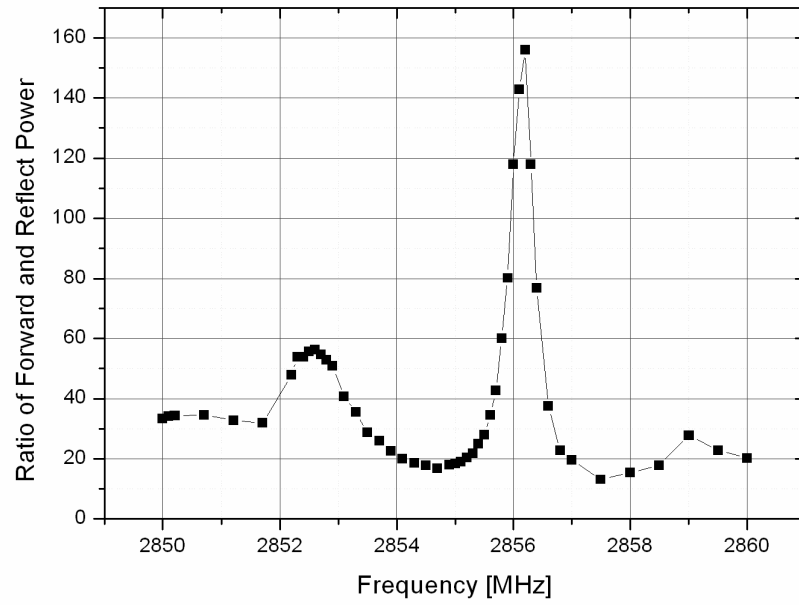


Figure 4.11: Measurement of the resonant frequency with a directional coupler in the klystron waveguide at cavity cooling temperature with 32.0 °C.

CHAPTER 5

Experimental Setup and Results

5.1 Photocathode RF Gun

Figures 5.1 and 5.2 show the experimental setup of the GTS at the PAL with a 1.6 cell photocathode S-band (2,856 MHz) RF gun with a solenoid containing 8 pancake-like coils. After the gun, a solenoid for the transverse emittance compensation is directly mounted with four ceramic keys for thermal isolation. A steering magnet with maximum magnetic field of 80 Gauss is installed inside of the solenoid bore. The solenoid magnetic field strength and field profile are measured based on the hall probe method [8]. The solenoid field measurement system, measured field profile and strength are

Chapter 5. Experimental Setup and Results

shown in Fig. 5.3. The steering magnet inside of the solenoid bore is shown Fig. 5.4 (a) and the measured magnetic field of the steering magnet is shown in Fig. 5.4 (b).

An integrating current transformer (ICT) to measure the beam charge is located immediately following the solenoid. After the ICT, there is a fluorescent screen to measure and monitor the beam profile. The screen is made of a 15 μm layer of YAG:Ce doped on 100 μm thick aluminum substrate to prevent charge build up, and is mounted on a vertically movable aluminum holder at 45° with respect to the beam axis. The position of the screen is 0.56 m from the cathode. A charge coupled device (CCD) camera is synchronized to the electron beam for a shot-to-shot measurement of the electron beam image.

At the downstream of the screen chamber, there is a spectrometer with 60° dipole magnet to measure the beam energy and the energy spread. When the spectrometer turns off, the beam goes straight to the downstream beam-line. When the spectrometer turns on, the beam goes to the beam analyzing screen. The beam analyzing screen is mounted on a fixed aluminum holder at 45° with respect to the beam moving direction. Figures 5.5 (a) and (b) show the drawings and the photograph of the spectrometer magnet and Fig. 5.5 (c) shows the estimated beam energy from applied current to the spectrometer. If the applied current is increased, the magnetic field of the spectrometer is also increased. The beam energy is in proportion to the applied magnetic field strength on the spectrometer.

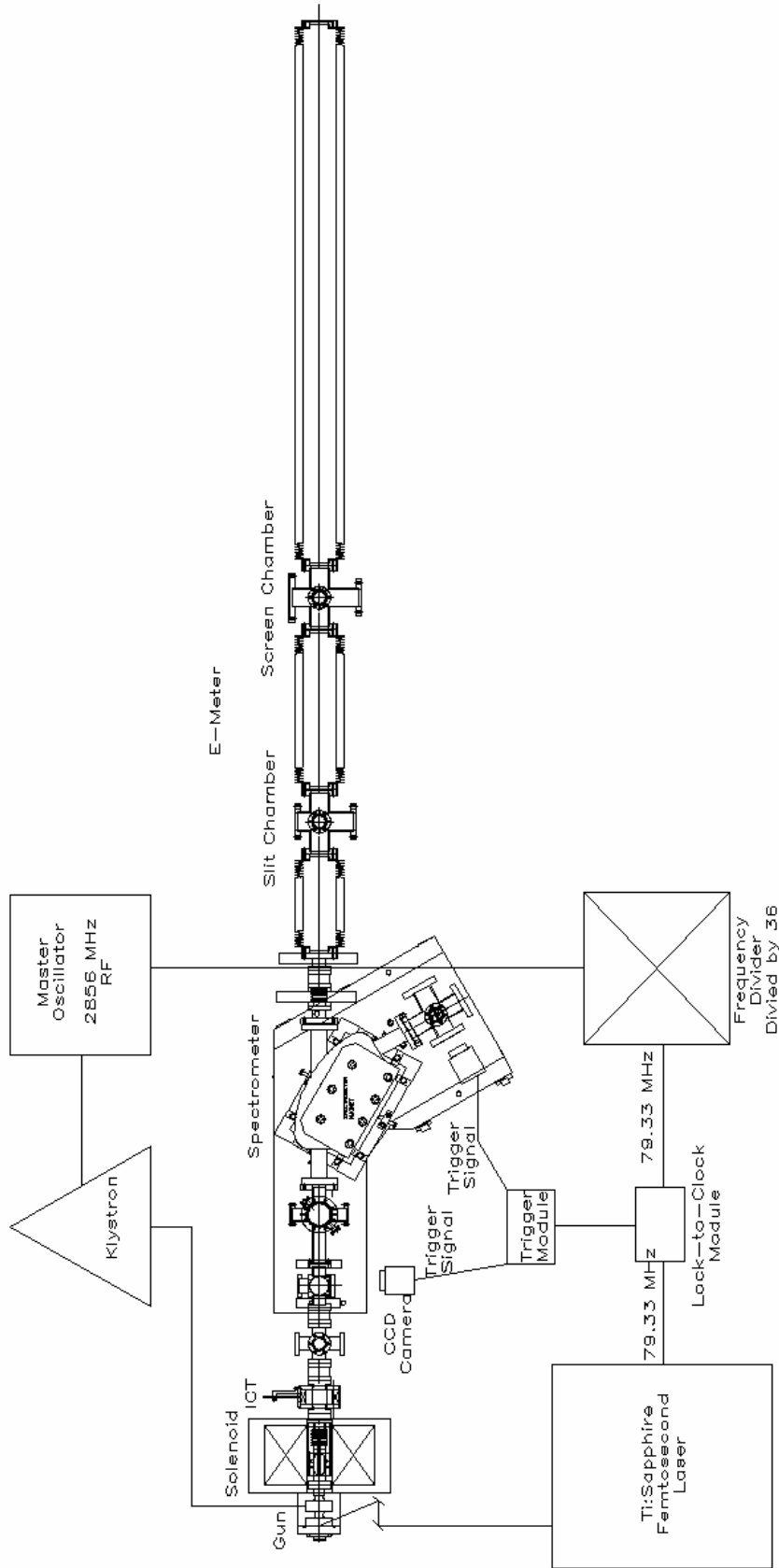


Figure 5.1: Schematic diagram of the gun test stand (GTS) at the PAL.

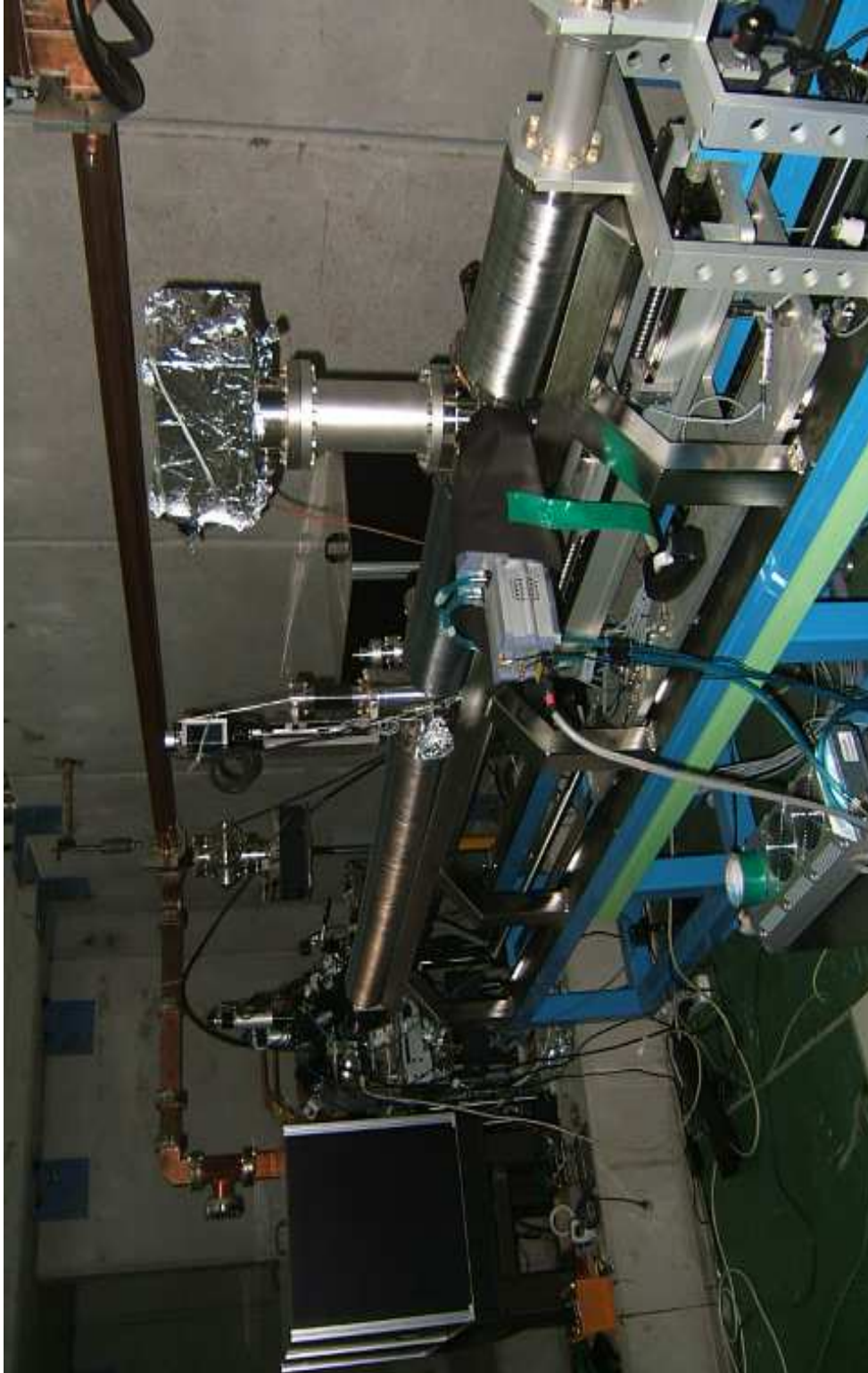


Figure 5.2: Photograph of the gun test stand (GTS) at the PAL.

Chapter 5. Experimental Setup and Results

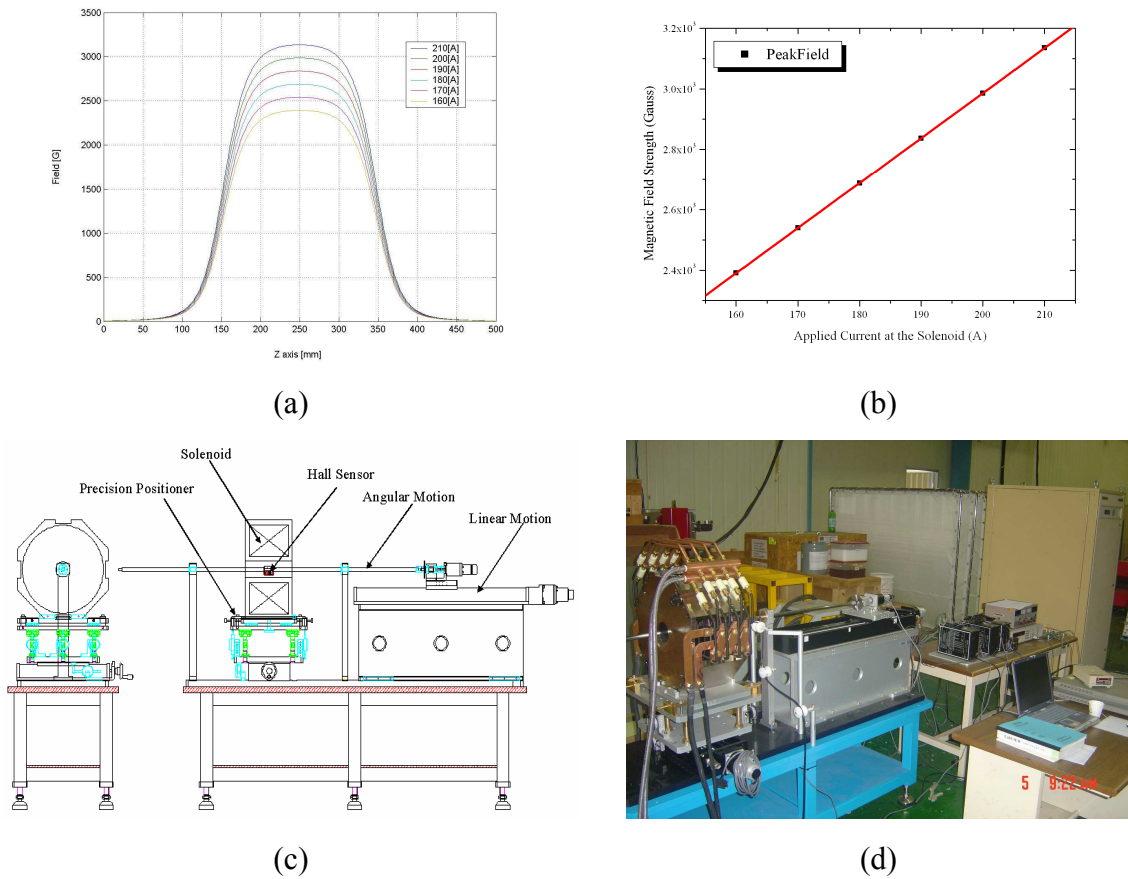
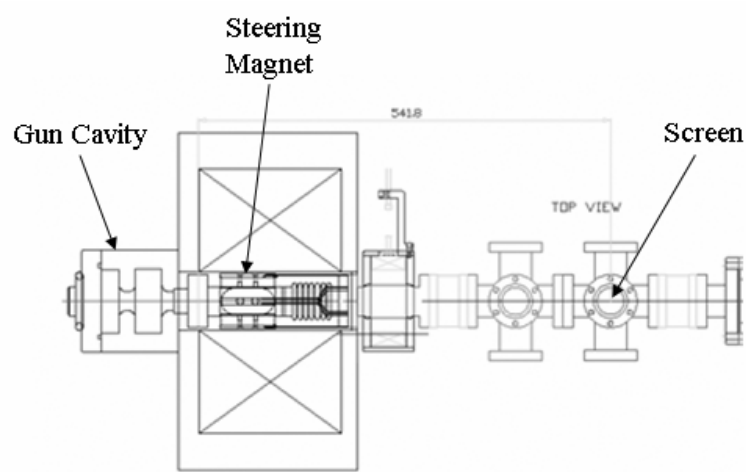
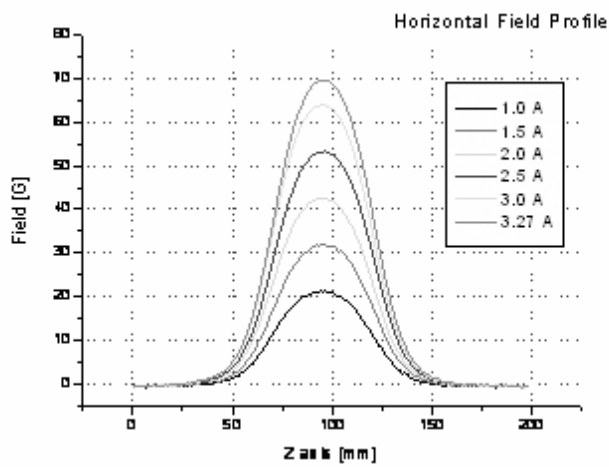


Figure 5.3: The solenoid for the emittance compensation: (a) the measured field profile of the solenoid on axis, (b) the graph of the applied current on the solenoid vs. peak solenoid field, (c) schematic diagram of the solenoid field measurement device based on hall-probe measurement, (d) the photograph of the solenoid field measurement device.

Chapter 5. Experimental Setup and Results



(a)



(b)

Figure 5.4: (a) The schematic diagram of the steering magnet inside of solenoid bore and (b) the graph of the applied current vs. measured magnetic fields of the steering magnet.

Chapter 5. Experimental Setup and Results

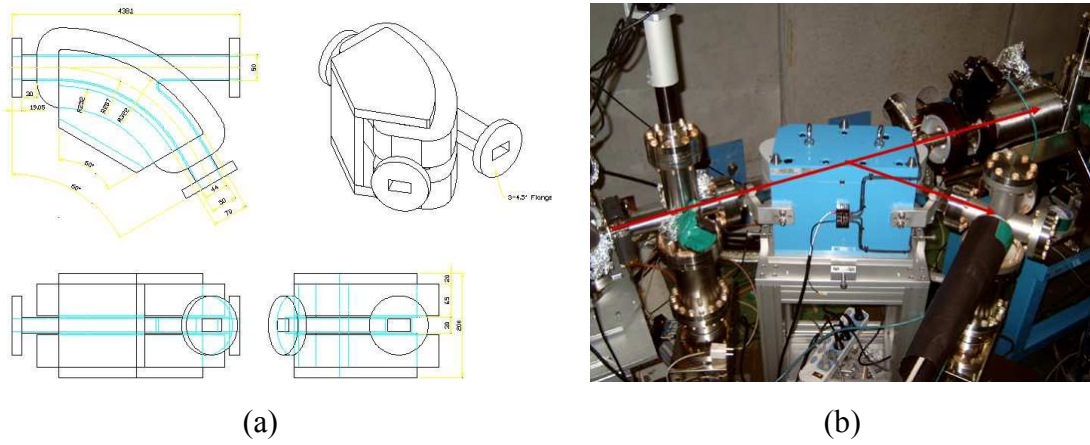


Figure 5.5: The spectrometer magnet for beam energy measurements: (a) The drawing of the spectrometer magnet, (b) the photograph of the spectrometer, (c) the graph of the applied spectrometer magnet current vs. beam energy based on the measured spectrometer field.

5.2 Emittance Meter

We have designed the emittance meter (E-Meter) which has a movable slit chamber and a screen chamber along the beam axis with independent bellows. The transverse emittance evolution after the solenoid in a drift space predicted by the emittance compensation theory and simulation [13, 22-24] is measured with this E-Meter. The E-Meter is shown in the right side of Fig. 5.6. The E-Meter consists of a slit chamber with 4-axis moving stage and a screen chamber to measure the beamlet size. The slit chamber is equipped with a single slit plate to make beamlet and a YAG screen to measure the main beam size [30, 44-49]. The screen chamber is equipped with a YAG screen to measure the size of the beamlet made by the slit plate. The distance from the slit chamber to the screen chamber can be adjusted according to the beam divergence. If the beam has a large divergence, the distance should be short, and vice versa, to make an optimized image size on the screen. The position of the slit plate chamber and the screen chamber cameras can be monitored by two CCD, independently. The plates for single slit are made of tungsten with 0.5 mm thickness. There are three slits in the plate, which are fabricated by high power laser micro-drilling with slit sizes of 30, 40, and 50 μm , respectively, as shown in Fig. 5.7 (a). Figures 5.7 (b) and (c) show magnified photographs of the fabricated slit plate of width 30 and 40 μm , respectively. The slit plates in the #2 screen chamber are vertically mounted with a stepping motor to be changeable at the specific experimental position. The sizes of the slit are determined by considering the signal to noise ratio of the beamlet on the screen and the acceptance angle when the beam goes through the slit plate [30]. We have designed to align the slit plate and the screen by the 4-axis moving stage of a goniometric motion, a rotary

Chapter 5. Experimental Setup and Results

motion, x and y linear motions with high accuracy stepping motor on the slit chamber, respectively. Scanning the single slit is used usually with y directional linear motion which requires a precision moving control for the full measurement of small beam size [50].

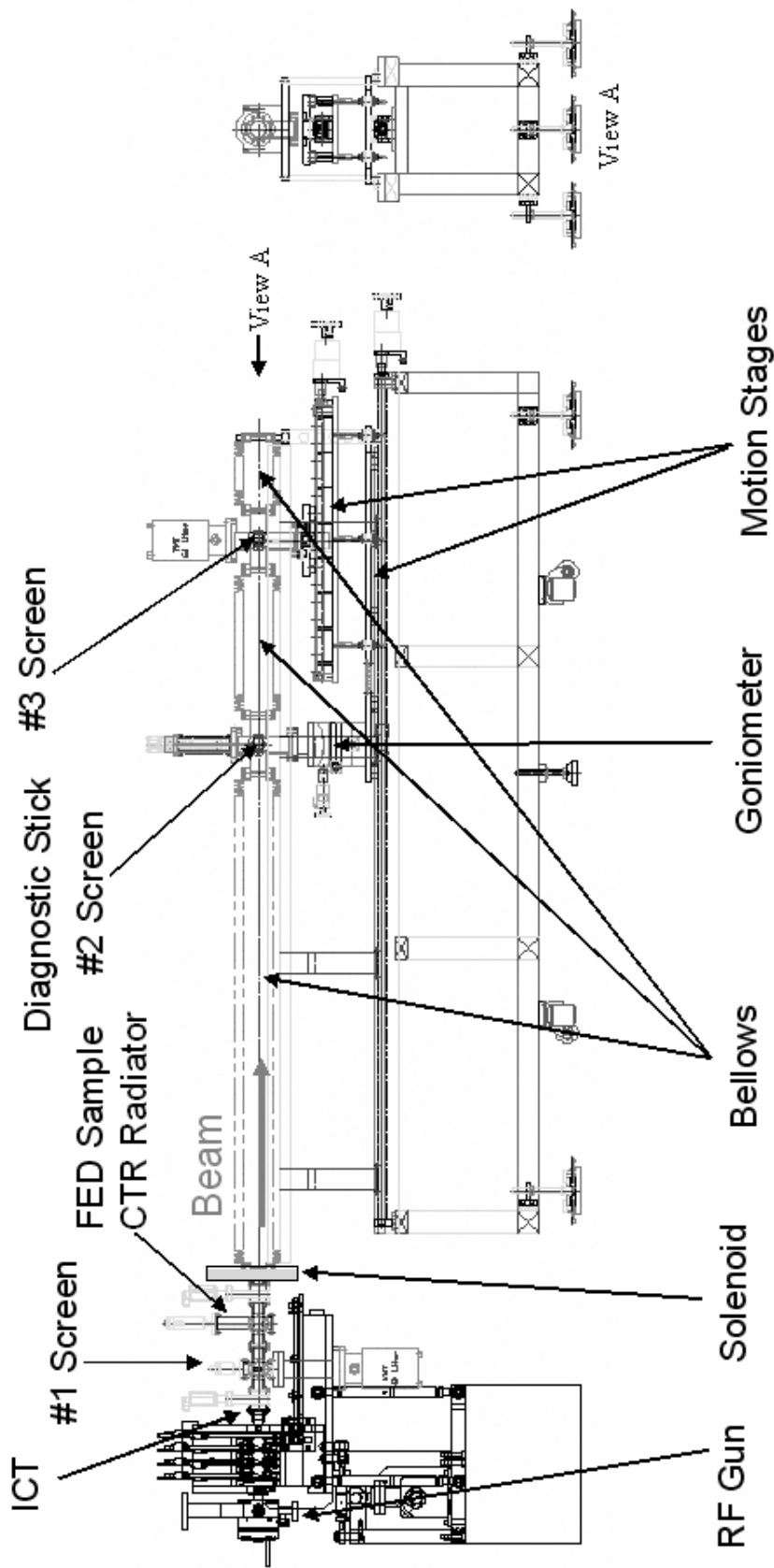


Figure 5.6: The diagram of the emittance measurement setup for the measurement of the beam

Chapter 5. Experimental Setup and Results

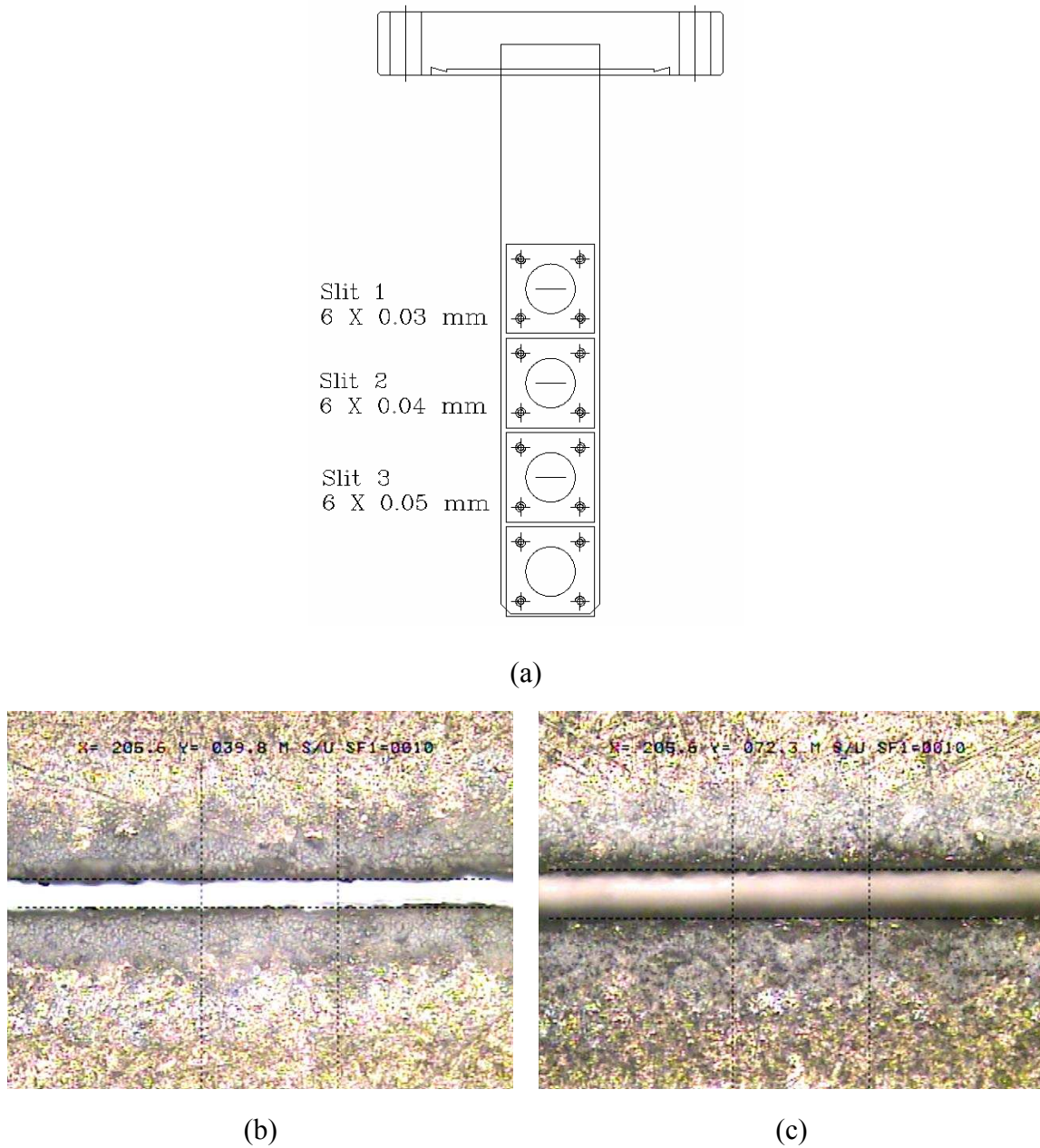
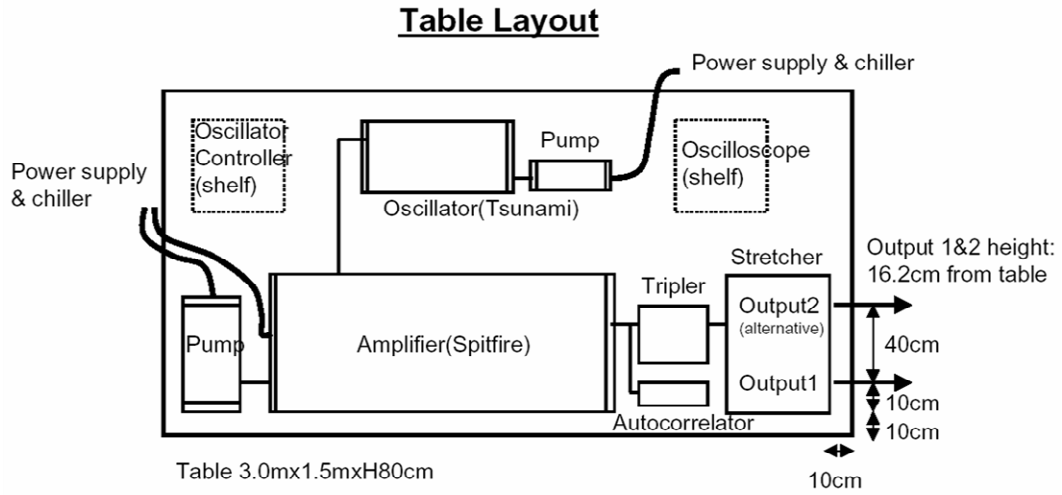


Figure 5.7: The schematic diagram of the single slit plates and its holder (a). The slit width is 30, 40, and 50 μm , respectively. The photographs of the fabricated slit plate with 30 μm (b) and 40 μm (c).

5.3 Laser System

The laser system consists of an active mode-locked Ti:Sapphire oscillator (Tsunami, Spectra-Physics), a regenerative amplifier (Spitfire Pro, Spectra-Physics), a custom designed third harmonic generator (THG), and a custom designed UV stretcher system. Figure 5.8 (a) shows a table layout of the laser system for the PC RF gun. The laser system for the RF PC gun is installed in a clean room where the temperature is dynamically controlled within 0.5 °C for stable operation as shown in Fig. 5.8 (b). The laser oscillator is operated at a frequency of 79.33 MHz by frequency divided by 36 from the master oscillator of 2,856 MHz. The lock-to-clock module is used to synchronize between a frequency of 79.33 MHz by frequency divided by 36 from the master oscillator of 2,856 MHz and a frequency of 79.33 MHz of the laser oscillator. The oscillator output is phase-locked with a reference 79.33 MHz by dynamically adjusting the cavity length of the oscillator with a piezo mirror by high voltage signal of the lock-to-clock module. The schematic diagram of the synchronization between the laser and the master oscillator is shown in Fig. 5.9.

Chapter 5. Experimental Setup and Results



(a)



(b)

Figure 5.8: (a) Table layout of the laser system for PC RF gun and (b) the photograph of the laser system.

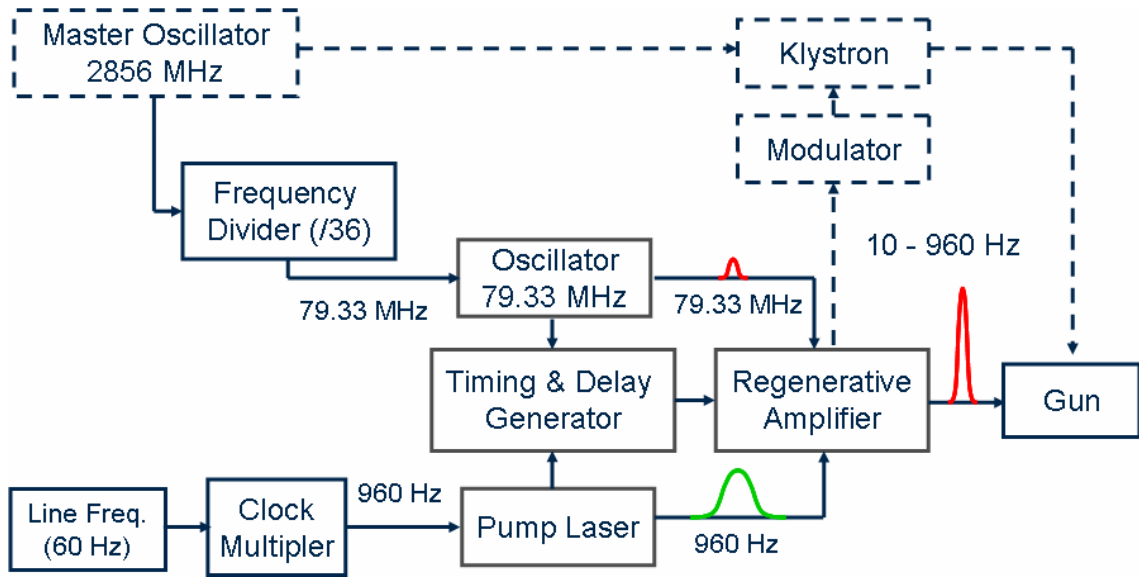


Figure 5.9: The schematic diagram of the synchronization between the laser and the master oscillator.

The timing jitter is measured to be within an rms value of 126.5 fs by a phase detection method with the digital sampling oscilloscope of Tektronix 11801B as shown in Fig. 5.10 [7]. The measured energy stability of the oscillator output is $< 1\%$ peak to peak as shown in Fig 5.11. From the oscillator, 105 fs width with a full width at half maximum (FWHM) value, a 800 nm wavelength pulse is generated with 79.33 MHz repetition rate. These laser pulses are amplified in the regenerative amplifier up to about 2.5 mJ with 1 kHz repetition rate. After the regenerative amplifier, the amplified laser pulse is injected into the THG composed of a pair of frequency conversion non-linear crystals to obtain 266 nm UV light with maximum energy of 250 μ J. The UV laser pulse still has an ultra short pulse width. An UV pulse stretcher with a pair of prisms is installed in order to stretch the pulse width of the UV laser to 10 ps FWHM. In addition, the UV pulse stretcher has a capability to change the pulse duration of the UV laser from 1 ps (FWHM) to 10 ps (FWHM). A home-made cross correlator with a BBO

Chapter 5. Experimental Setup and Results

crystal is installed in order to measure the pulse width at the UV region using the cross correlation method [7]. Figure 5.12 (a) shows the layout of the THG optics, the UV pulse stretcher, and the cross correlator. Figure 5.12 (b) shows the measured pulse length of the stretched UV. Table 5.1 lists the specification of the laser for the PC RF gun.

Table 5.1: Specifications of the laser for the PC RF gun.

Parameter	Value	Unit
Oscillator wavelength	800	nm
Oscillator Power	2.5	W
Oscillator frequency	79.33	MHz
wavelength at UV	266	nm
Energy at UV	250	μ J
Pulse width	10	ps, nominal
Repetition rate	10-1,000	Hz
Timing jitter	< 130	fs
Energy stability	1	%, peak-to-peak

Chapter 5. Experimental Setup and Results

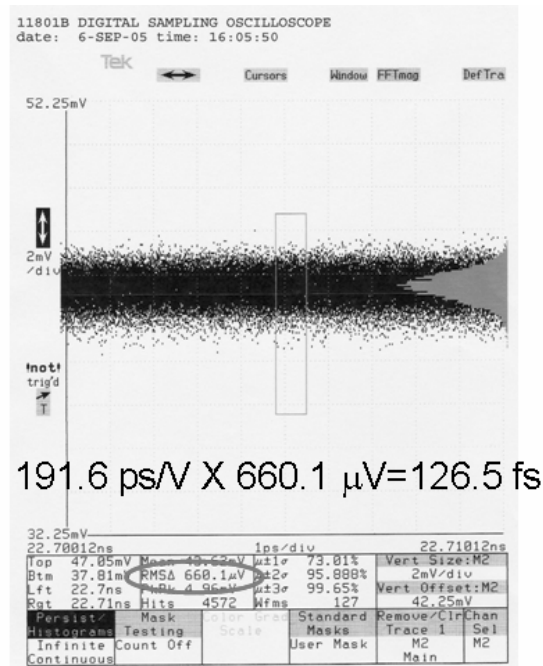


Figure 5.10: The timing jitter is measured to be within an rms value of 126.5 fs by a phase detection method with Tektronix 11801B.

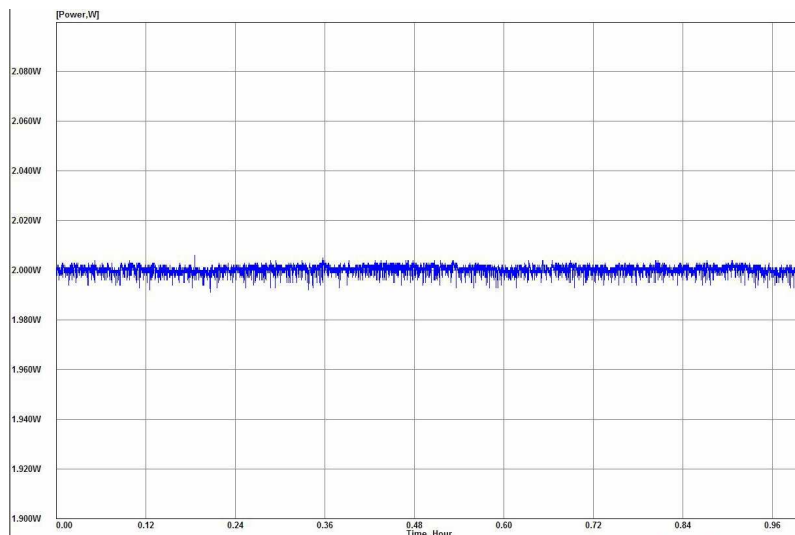
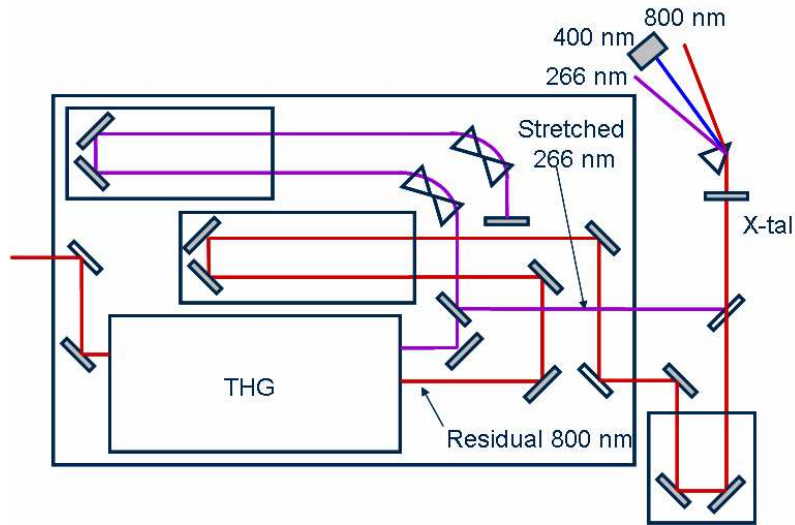
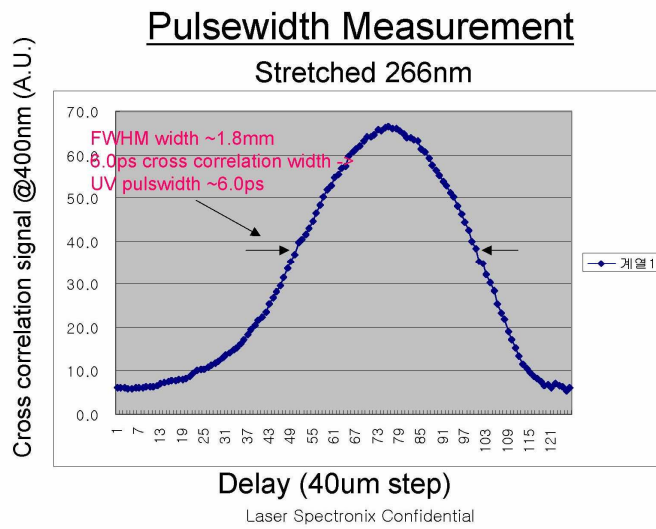


Figure 5.11: Measured energy stability of the oscillator output is < 1 % peak to peak.

Chapter 5. Experimental Setup and Results



(a)



(b)

Figure 5.12: The optics layout of the THG, the UV stretcher, and the cross correlator (a) and the measured UV pulse length (b) with the home-made cross correlator.

5.4 Experimental Results

5.4.1 Beam Charge and Quantum Efficiency versus Laser Injection Phase

The beam charge and the quantum efficiency are measured in connection with the laser injection phase at four different laser energies by using the ICT. The zero phase can be defined as a starting phase of the beam emission from the cathode measured by slowly increasing the laser injection phase. Bergoz Instrumentation made ICT has a 5:1 pulse output ratio and a sensitivity of 5 V·s/C in a 50 Ohm termination. The ICT signal is monitored on the oscilloscope and the beam charge is evaluated with its sensitivity [51]. For example, the beam signal of 20 ns (FWHM) width with 100 mV peak amplitude indicates the beam charge of 400 pC.

The photoelectron current can be described by [52, 53],

$$J = aI \left(h\nu - \phi_0 + b\sqrt{\beta E} \right)^2, \quad (5.1)$$

where a is a constant related to the material properties, I is the laser intensity, $h\nu$ is the incident photon energy with 4.67 eV at 266 nm wavelength, ϕ_0 is the work function at zero field with 4.65 eV for copper, $b = \sqrt{e/4\pi\epsilon_0}$, β is the field enhancement factor, and $E = E_0 \sin\theta$ is the applied electric field at the cathode varied with the laser injection phase, θ . The quantum efficiency (QE) is proportional to the ratio between the photoelectron current and the laser intensity as given by [52-54]

$$\text{QE} = a \left(h\nu - \phi_0 + b\sqrt{\beta E_0 \sin\theta} \right)^2. \quad (5.2)$$

Chapter 5. Experimental Setup and Results

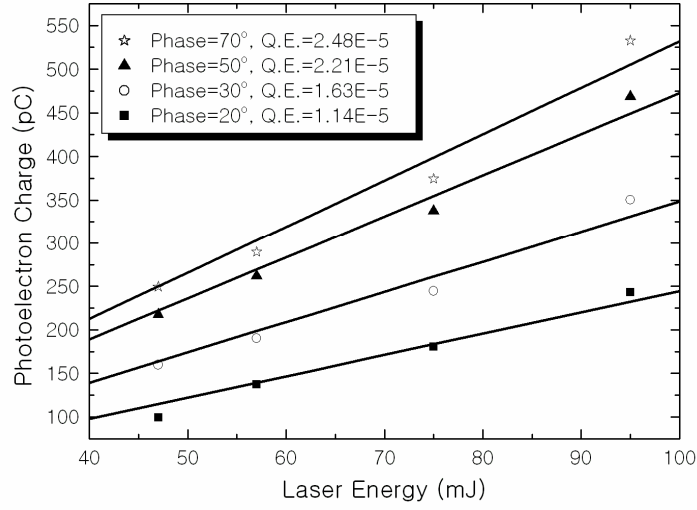
According to Eq. (5.2), it can be represented that \sqrt{QE} is directly proportional to the field on the cathode, $\sqrt{E_0 \sin\theta}$. The photoelectron from the copper cathode is dominated by different laser injection phases and intensities. The beam charge as a function of the laser injection phase is measured by adjusting the RF phase shifter. The laser spot size with the transverse flat top on the cathode surface is about 4 mm in a diameter. In this measurement, the electric field on the cathode surface is 40 MV/m with 1.8 MeV beam energy. Figure 5.13 (a) shows the measured QE with different laser injection phases. As shown of the Fig. 5.13 (b), the experiment is in a good agreement with Eq. (2) at the constant E_0 . The highest measured QE is 2.48×10^{-5} at a laser injection phase of 70° .

At the various electric fields on the cathode the quantum efficiency are measured about different laser injection phases. The beam energy is proportioned applied electric field on the cathode. At the low energy electron beam the peak of the quantum efficiency along to laser injection phase is clearly appeared two peaks with almost same amplitude as shown in Fig 5.14 (b). As the increasing the beam energy, the peaks are shifted to 90° and become smaller that implies the different dynamics of the beam in the cavity along to different beam energy. These phenomena are shown in Fig. 5.14. The ratios of the two peaks of the quantum efficiency are plotted along to the applied electric fields as shown in Fig. 5.15. The ratio is decreased as increase the applied electric fields. In relatively high electric field, these double peaks are not appeared due to the smearing out the second peak of the quantum efficiency. But in relatively low energy beam, these double peaks are clearly appeared. Thus in low energy beam, beam dynamics in the cavity can be deduced by the PARMELA simulation as shown in Fig.

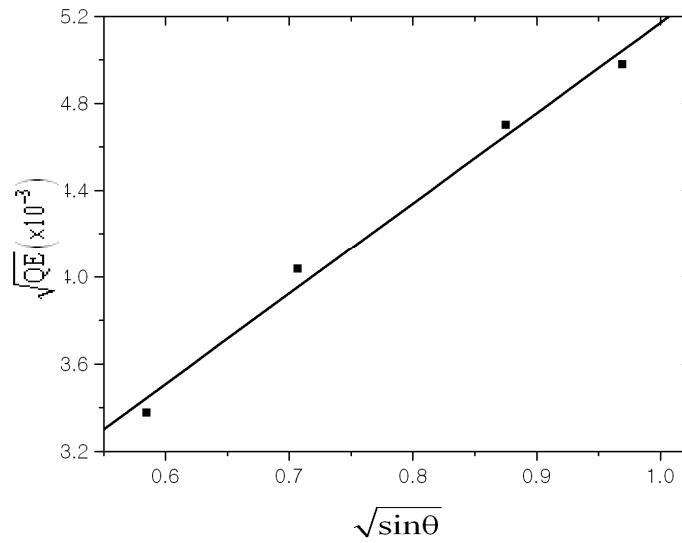
Chapter 5. Experimental Setup and Results

5.16. As change the laser injection phase, the beam energy is quite large different phase. On the proper phase, the beam is accelerated at the both cell. On the improper phase, the beam is decelerated at the both iris in the cavity. These phenomena are explained low energy beam dynamics such as phase scan of the low energy beam.

Chapter 5. Experimental Setup and Results



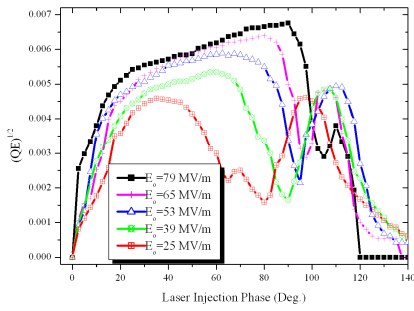
(a)



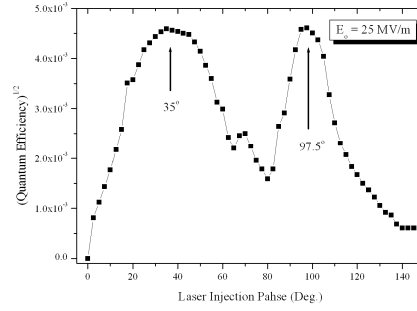
(b)

Figure 5.13: Quantum efficiency vs. different laser injection phase (a) and \sqrt{QE} vs. $\sqrt{\sin\theta}$ (b). The measured quantum efficiency is 1.63×10^{-5} at a laser injection phase of 30° with minimum beam emittance by the beam dynamics simulation.

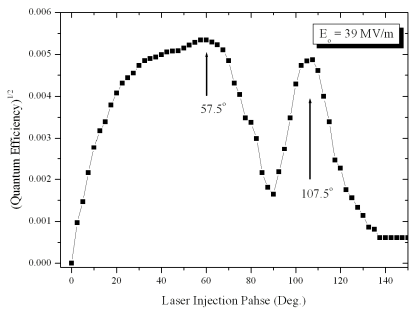
Chapter 5. Experimental Setup and Results



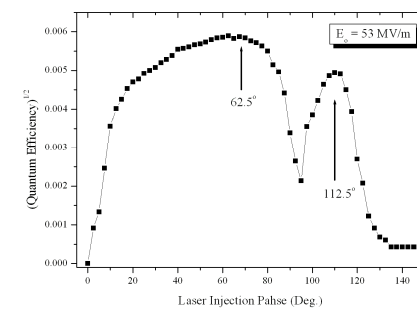
(a)



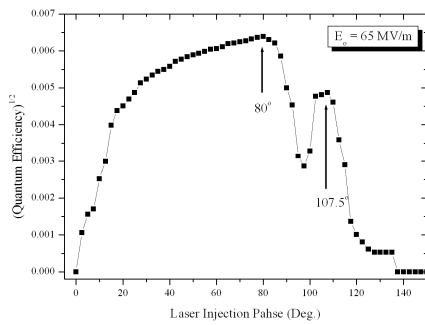
(b)



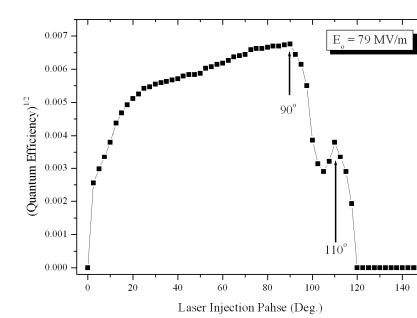
(c)



(d)



(e)



(f)

Figure 5.14: The laser injection phase vs. square root of the quantum efficiency about various electric field strengths at the cathode. The square root of the quantum efficiency peak is shifted along to the field strength.

Chapter 5. Experimental Setup and Results

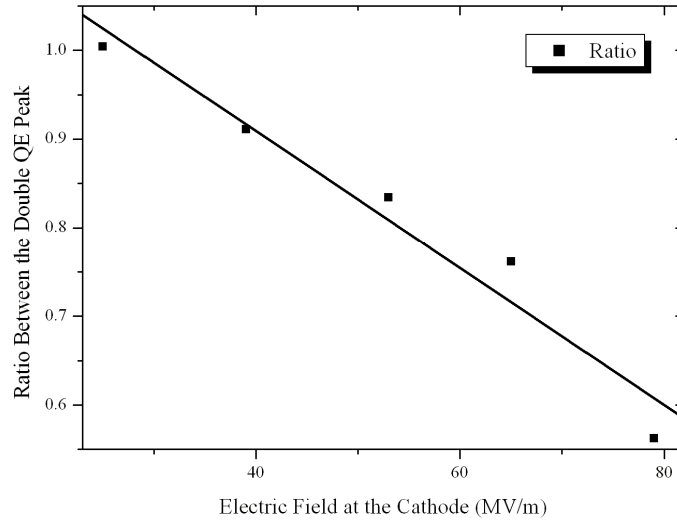


Figure 5.15: The electric field strength vs. the ratio between double peaks of the square root of the quantum efficiency. The peak ratio is linearly decreased along to increasing of the field strength.

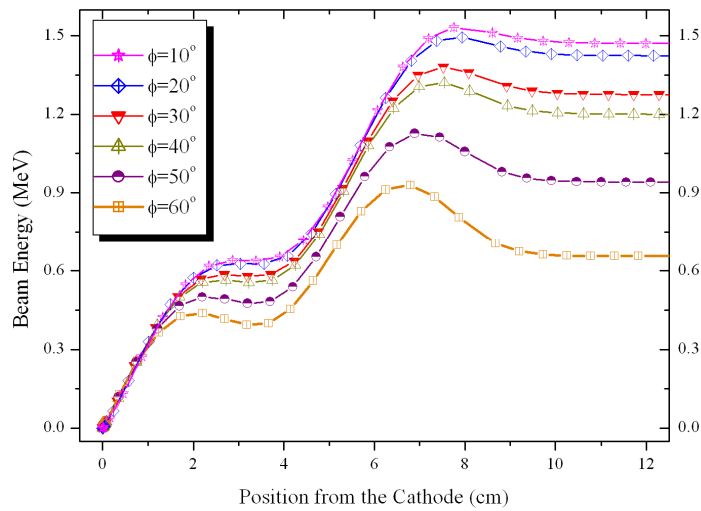


Figure 5.16: The position from the cathode vs. the beam energy about various laser injection phases at the electric field strength of 45 MV/m.

Chapter 5. Experimental Setup and Results

We have tried to measure the photocurrent and the QE by using p-polarized and s-polarized laser for oblique incidence. In analytical calculation for the perfect surface condition, the QE by using p-polarized laser is 5 times larger than using s-polarized laser at an incidence angle of 67.5° with respect to the cathode normal direction [55]. Since the cathode surface is not in the perfect condition, however, the difference of beam charge and the QE with laser polarization is smaller the ideal condition as shown in Fig. 5.17. The data is obtained with the laser pulse power of $90 \mu\text{J}$ with 4 mm spot size on the cathode. The QE for the p- and the s-polarized laser is 3.11×10^{-5} and 1.97×10^{-5} , respectively, at the cathode electric field of 45 MV/m.

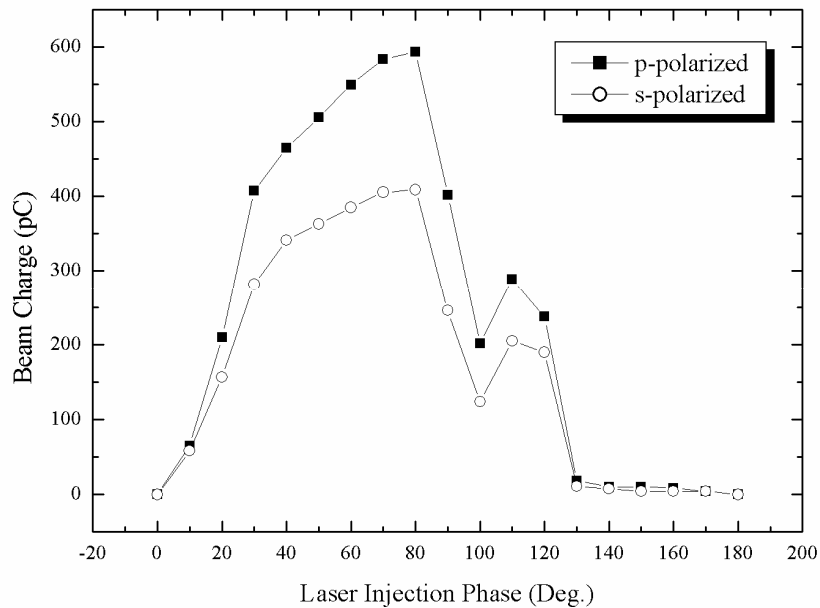


Figure 5.17: Photoelectron charge vs. laser injection phase using the p- and the s-polarized lasers at a field of 45 MV/m on the cathode surface.

Chapter 5. Experimental Setup and Results

The polarization of the laser is varied along the waveplate angle. The laser reflectivity about the waveplate angle is measured by the power meter. The polarization of the laser varies due to the waveplate angle, the reflectivity of the cathode changes due to polarization change. The quantum efficiency of the cathode is inversely changed about the reflectivity of the laser as shown in Fig. 5.18. The ratio of the reflectivity between the s-polarization and the p-polarization is measured 2.46. But the ratio of the quantum efficiency at the s-polarization and p-polarization is measured 1.38. If the cathode condition is perfected, the ratio of quantum efficiency reaches the ratio of the reflectivity. These experiments are performed with the field strength of 65 MV/m at the cathode at 30° laser injection phase.

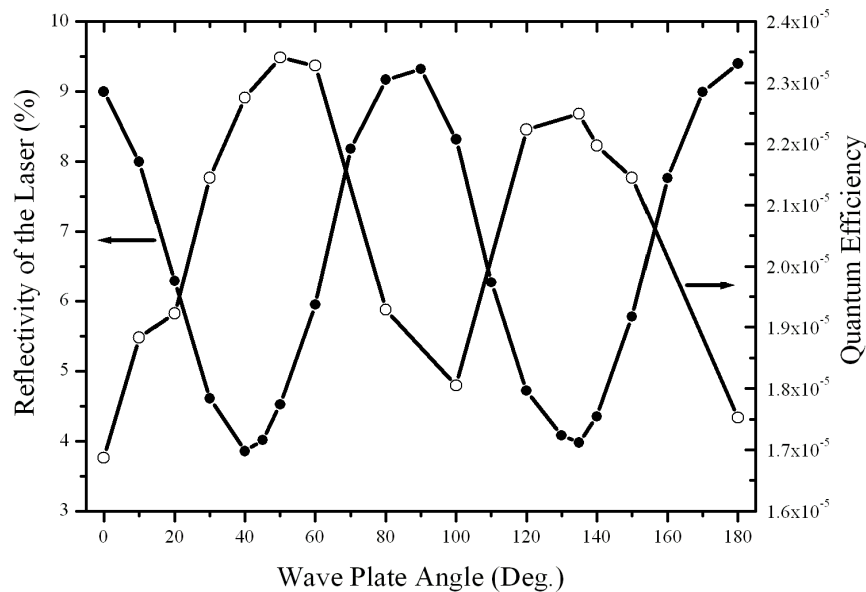


Figure 5.18: The measured waveplate angle vs. the reflectivity of the laser (solid circle) and the waveplate angle vs. the quantum efficiency (empty circle).

5.4.2 Dark Current Measurement

After the photocathode RF gun is brought into the operation, we have observed photo currents as well as dark currents. The dark current is induced by field emissions due to strong electric fields on the cathode surface. The dark current emission can be classified into three steps. First, the dark current is rapidly increased from the instantaneous turn-on of the RF power for filling the electromagnetic field into the gun cavity. The filling time of the gun cavity is about 0.7 μ s. Laser injection time is within the stable region between the filling of the fields into the cavity and just before turn-off of the RF power. Second, the dark current from the gun cavity keeps saturated until the RF power is turn off, and then quickly vanishes at the moment of turn-off. The relation of the field emitted current (I_F) and the applied electric field (E) on the cathode given by [56],

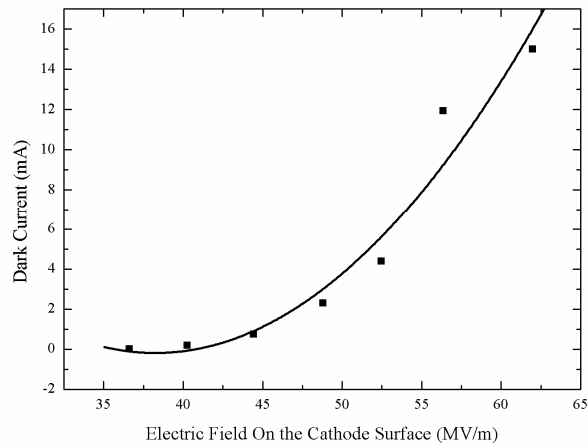
$$I_F = \frac{1.54 \times 10^{-6} \times 10^{4.52\phi^{-0.5}} A_e \beta^2 E^2}{\phi} \exp\left(-\frac{6.53 \times 10^9 \phi^{1.5}}{\beta E}\right) \quad (5.3)$$

where ϕ is the work function of the copper, A_e is an effective emitting area, and β is a field enhancement factor. The vertical axis of Fig. 6 is “Dark Current (mA)”. The dark current at a 62 MV/m electric field on the cathode is measured a 15.1 mA. The numerical value of β for our cavity surface can be obtained by Fowler-Nordheim fitting [57] which is 120 as shown in Fig. 5.19 (b). Generally, the amount of the dark current is connected with surface roughness and vacuum level in the cavity. The dark current is lower for lower field enhancement factor if the RF field is constant. The enhancement factor is fair around the typical value of 120. Energy of the dark current beam is slightly below the photo-current energy due to random acceleration process of the dark current when the RF power is on. The dark current is built up after filling of the field in the cavity and its time duration is in the order of a few μ s. But the time structure

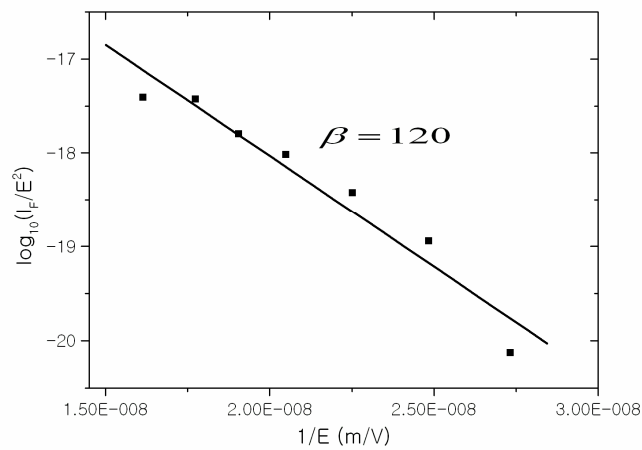
Chapter 5. Experimental Setup and Results

of the photo current is similar to the laser profile and the duration is about 10 ps. The dark current is quit low in the operation with low power RF at this time. The dark current can be reduced an aging process of the cavity with high power RF.

Chapter 5. Experimental Setup and Results



(a)



(b)

Figure 5.19: (a) The electric field on the cathode vs the dark current. The dark current is squarely proportional to the electric field on the cathode. (b) The field enhancement factor by Fowler-Nordheim fitting is 120.

5.4.3 Laser Injection Phase versus Energy

The beam energy and the energy spread at position 1.2 m from the cathode are measured by a spectrometer magnet which consists of a 60° bending magnet and a screen for the beam profile measurement. The distance between the spectrometer magnet and the screen is 0.5 m. If the beam is entered with certain angle with respect to normal direction, an error of the beam energy come into the measured value. At our beam energy measurements the energy error is minimized by entering without the certain angle by two screens and two steering magnets in front of the spectrometer magnet. The energy spread of the beam is measured by the beam size on the screen. The beam energy can be estimated by measuring of the current of the spectrometer magnet when the beam is imaged at the center position on the screen. The beam energy can be analyzed by the spectrometer field integral [58],

$$E[GeV] = \frac{0.29979}{\theta} \int B d\ell [T \cdot m / rad], \quad (5.4)$$

where $\int B d\ell$ is the integrated dipole field and θ is the geometrical bending angle.

The beam energy with the laser injection phase is measured by the spectrometer magnet as shown in Fig 5.20. The laser injection phase with the maximum energy is measured to be 1° that is a correspondence between the simulation and the experimental result in low field gradient [58]. When the laser injection phase is changed by a phase shifter, the beam charge and the beam energy are changed. Thus the solenoid current for the beam focusing on the screen should be simultaneously changed. The relative energy spreads at the laser injection phase of 10° and 30° are measured to be 0.67 %, 2.20 % rms, respectively. The beam energy is decreased as the laser injection phase is increased, but the energy spread increases as the beam energy decreases. Figure 5.21 shows the beam

Chapter 5. Experimental Setup and Results

energy as a function of the field gradient on the cathode surface at the laser injection phase of 1° .

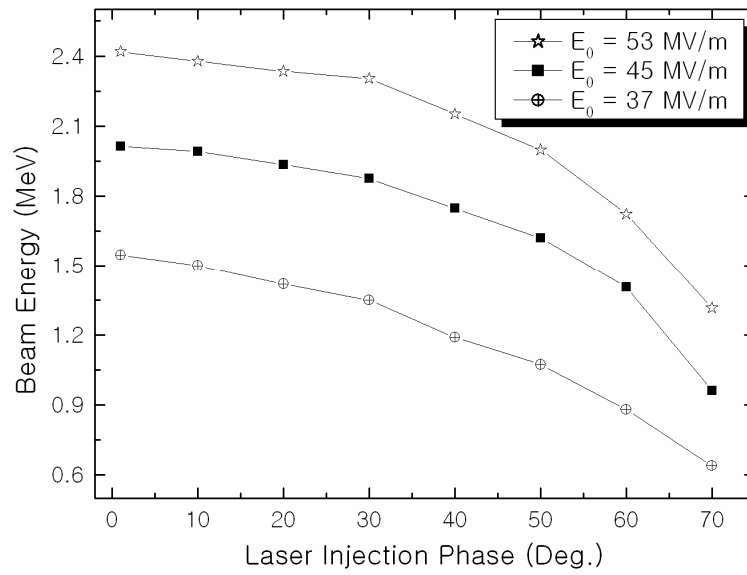


Figure 5.20: The beam energy as a function of the laser injection phase with different field gradients.

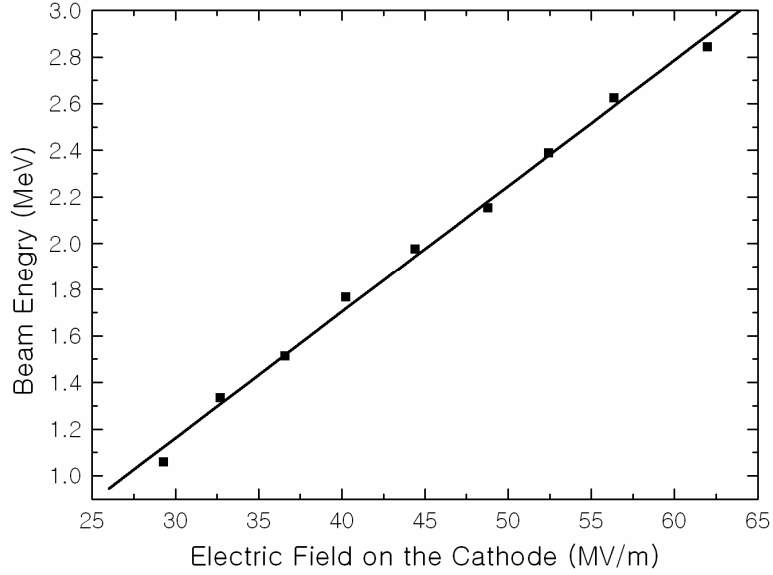


Figure 5.21: The beam energy as a function of the field gradient in the RF gun.

5.4.4 Measurements of the Transverse Emittance Evolution

The transverse dynamics of charged particle beams is described by the following equation [23, 59]

$$\sigma'' + \sigma' \left(\frac{\gamma'}{\beta^2 \gamma} \right) + K_r \sigma - \frac{\kappa_s}{\sigma \beta^3 \gamma^3} - \frac{\varepsilon_n^2}{\sigma^3 \beta^2 \gamma^2} = 0, \quad (5.5)$$

where σ is the rms beam size, β and γ are the relativistic factors, K_r is the linear focusing channel, κ_s is the perveance, and ε_n is the normalized transverse emittance. The rms beam size and the normalized transverse emittance are damped as the beam is accelerated because of the non-vanishing σ' . This implies that the emittance oscillation is damped and the emittance can be frozen to a very low value under a proper condition.

Chapter 5. Experimental Setup and Results

The emittance compensation is a technique to reduce the normalized rms emittance of the beam at the photoinjector. The emittance compensation typically involves two complementary stages: the rotation of the phase space for each slice of the beam in the solenoid and the realignment of the slices and the fast acceleration in the booster. Essentially, the principle of the emittance compensation by solenoid is the balance between the repulsive forces due to the space-charge and the external focusing force. After the beam goes through the solenoid region, the beam is blowed up by the space-charge force if there is no booster linac to accelerate the beam to a relatively high energy [17, 22, 23]. Thus a booster is needed to accelerate the beam quickly to a relatively high energy region at which the phase space is frozen and the beam is emittance-dominated. To shift the second emittance minimum to the entrance of the booster linac where the beam is emittance-dominated, Serafini and Ferrario suggest a booster matching condition for the space-charge dominated beam from the gun to the booster [17, 23],

$$\begin{aligned}\sigma' &= 0, \\ \gamma' &= \frac{2}{\sigma} \sqrt{\frac{I_p}{2I_A \gamma}},\end{aligned}\tag{5.6}$$

where σ is the rms transverse spot size, I_p is peak current of the beam, $I_A = 17$ kA is the Alfvén current. The measurements of the beam emittance and the beam size evolution are essential to investigate the booster matching condition, as stated above.

In general, the quadrupole scan technique for beam emittance measurement is known to bring the over-estimation due to the purely space-charge dominated region [60]. We select the slit based emittance measurement method to avoid the away from the over-estimation. The slit plate creates a beamlet whose distribution is imaged on the screen,

Chapter 5. Experimental Setup and Results

located 0.71 m downstream from the slit. The width of the beamlet has a connection with a measure of the width of the transverse momentum distribution at the slit. To measure the emittance at each position on the beam axis of the slit from the cathode can be changed with a stepping motor without vacuum break. The beamlet yields the correlated beam divergence, and the rms transverse divergence is given by [30, 49],

$$\begin{aligned} x'_c &= \langle x - w \rangle / L, \\ \sigma' &= \sqrt{\frac{\langle x^2 \rangle}{L^2} - (x'_c)^2}, \end{aligned} \quad (5.7)$$

where L is the distance between the slit and the YAG screen, x is the measured beamlet size on the screen, and w is the slit width. Here the average is performed over the distribution in the measured beamlet. The beamlet size is measured about 10 times larger than the slit width to reduce the space-charge effect in the emittance measurement. The distance between the slit and the YAG screen can be changed for optimizing of the beamlet measuring on the YAG screen. The main beam size on the screen at the slit chamber and the beamlet size on the screen at the screen chamber are measured by the synchronized CCD camera. From the measured single beamlet size, the beam transverse divergence can be obtained to calculate the beam emittance from Eq. (5.7). Figure 5.22 shows the schematic diagram of the beam and the beamlet size measurement.

Chapter 5. Experimental Setup and Results

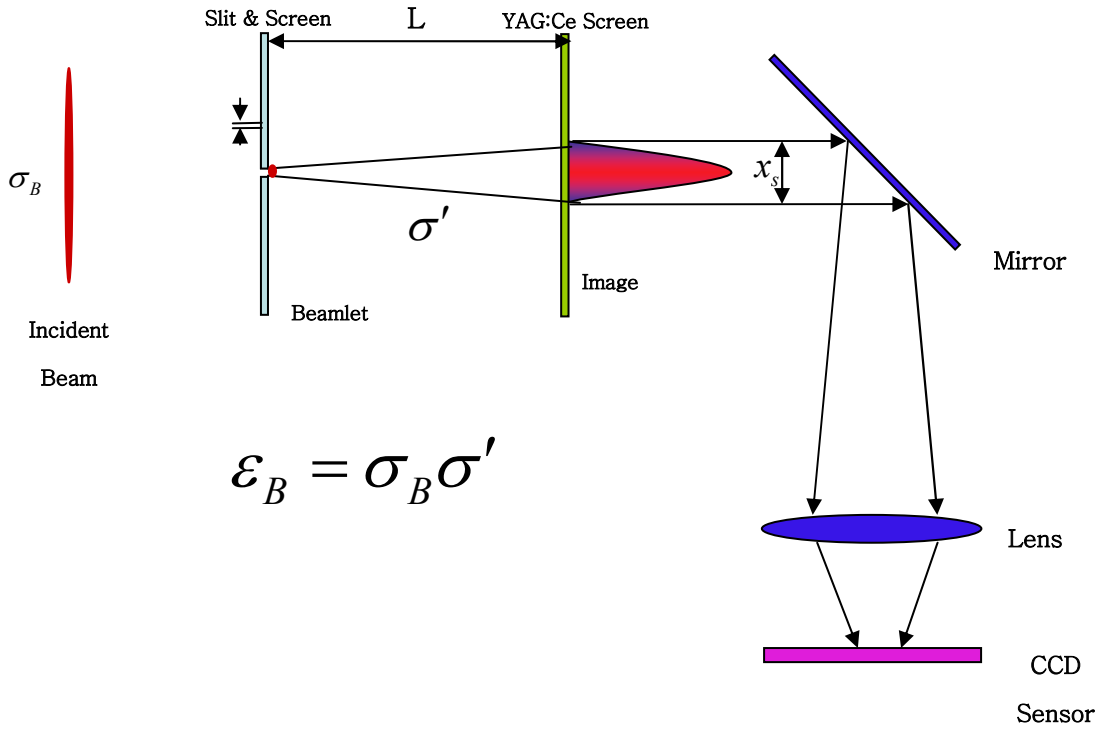


Figure 5.22: The schematic diagram of the beam imaging system from the incident main beam to the beamlet. The beamlet is made by the single slit.

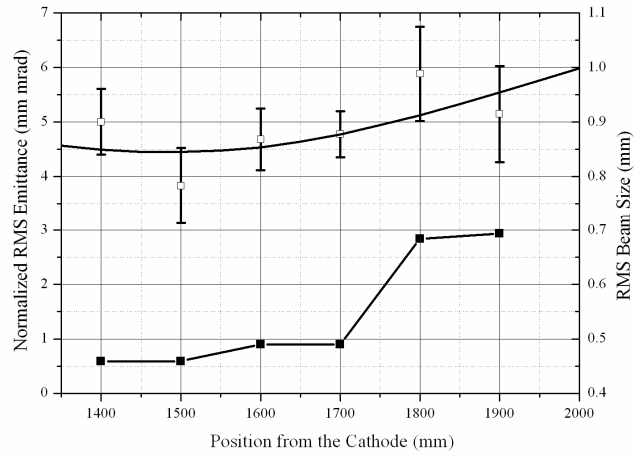
Chapter 5. Experimental Setup and Results

The evolution of the beam emittance and the beam size are shown in Fig. 5.23 (a). This experiment is performed with the condition of a 2.0 MeV beam energy, a solenoid field of 880 Gauss, and a 350 pC beam charge with 30° laser injection phase. The experimental result of the emittance evolution is in agreement with the simulation result about these beam conditions by the PARMELA code [34]. Figure 5.23 (b) shows the evolution of the beam size and the beam emittance of the beam with 3.7 MeV beam energy at the 30° laser injection phase. These experiments have 300 pC beam charge, 1.1 kG solenoid field strength. Table 5.2 lists the achieved beam parameters from the PC RF gun.

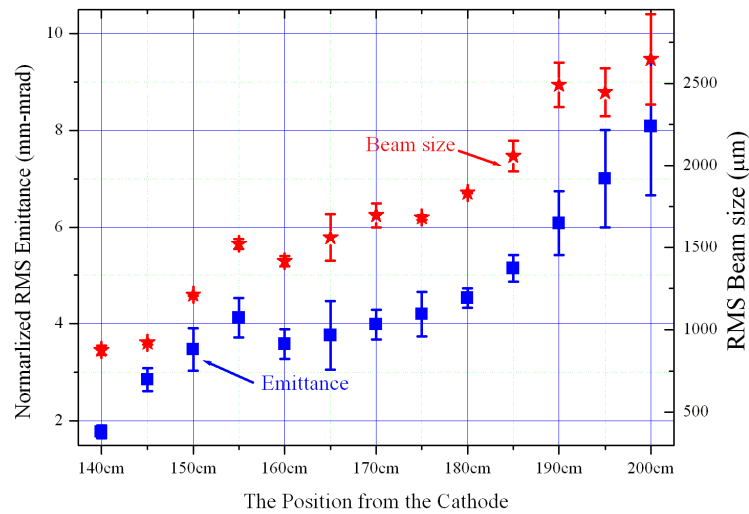
Table 5.2: Achieved beam parameters from the PC RF gun at the GTS

Parameters	Value	Unit	Note
Energy	3.7	MeV	Phase = 30°
Charge	550	pC	Max.
Beam spot size	0.79 ± 0.042	mm	rms, at 1.4 m from the cathode
Emittance	1.72 ± 0.29	mm-mrad	rms at 1.4 m from the cathode,
Energy spread	0.67	%	rms
Laser spot diameter	3	mm	Hard edge
Laser pulse length	5	ps	FWHM

Chapter 5. Experimental Setup and Results



(a)



(b)

Figure 5.23: (a): Simulations (solid line) by the PARMELA code and experimental results (empty square) of the beam emittance evolution. The beam size evolution is represented a square dot on the graph. These data are measured under the conditions of the beam is 2.0 MeV beam energy and 0.35 nC beam charge. (b): The beam emittance and the size evolution with 3.7 MeV beam energy and 0.3 nC beam charge.

CHAPTER 6

Conclusion and Future Work

6.1 Conclusion

The PC RF gun introduced here is the first product of the PC RF gun with the high-brightness in Korea. This gun is a starting point of the fourth generation light source for PAL XFEL which will provide many breakthroughs in various research fields. The measurements show a good performance of the PC RF gun by beam diagnostics at high power RF. The first experimental result of the emittance evolution shows a good agreement with the simulation one. At the future experiments, the booster matching point will be investigated by our experiments to optimize the emittance compensation

Chapter 6. Conclusion and Future Works

process i.e., by the emittance characterizations for various longitudinal position which will be performed by the E-Meter. This gun will be used for the FED [9-12] and the fs-FIR facility [61, 62]. Some weak points of this PC RF gun such as a beam axis alignment and the dark current problem will be modified in next gun fabrication for the PAL XFEL.

The results of the cavity design by the cavity simulation, the analytical calculation, tuning, fabrication, microwave measurements, and high power microwave test for development of the PPI are studied at the GTS. The photo-cathode RF gun at the GTS is commissioned by the microwave and the beam measurements for development of the PPI. The ultimate goal of the PAL XFEL photo-injector is to produce a 1 nC electron beam with a transverse normalized rms emittance of less than 1 mm-mrad. For achievement up to this parameter, we attempted the development of the photo-cathode RF gun at the gun test stand in the PAL. At the GTS, the best normalized transverse rms emittance at the 1.4 m position from the cathode attained 1.72 ± 0.29 mm-mrad at the 0.3 nC beam charge with 3.7 MeV beam energy. At this time, the beam spot size is measured 0.79 ± 0.042 mm. In order to achieve the ultimate goal, it is necessary to have experimental measurements of the emittance evolution at various conditions. Thus, measurements of the emittance evolution are performed and the result shows a good agreement with the simulation.

6.2 Future Work

The PPI development for the PAL XFEL will be continuously progressed based on these experimental results. The development of the GTS has been favorably progressed

that gives us experiences of the cavity designing, the microwave parameter measurements, the photocathode RF gun fabrication, tuning, and the beam diagnostics.

6.2.1 Issues of the Beam Dynamics Study

The beam dynamics studies in the cavity and in the drift region are carried through the charge scan and the emittance evolution measurements as computational and experimental approaches, respectively. Experiments of the emittance evolution have been practiced under the low energy condition (less than 3.7 MeV). However, in the emittance optimized simulation, the emittance oscillation is clearly appeared under sufficiently high energy (higher than 4.5 MeV). We have already measured the emittance evolution, but the oscillation of the emittance at the low energy is not appeared because the energy is not enough to measure the emittance oscillation. The beam energy should be increased to higher than 4.5 MeV beam energy at the exit of the gun cavity.

We have used the laser beam with an oblique incident to produce the photo-electron beam. The time slew effect of the beam is given by the oblique incident laser beam. Thus, the electron bunch length is increased several times larger than laser pulse length as a function of the laser spot size on the cathode. It changes the space charge force in the electron bunch. The normal incident of the laser beam is worth consideration in the bunch length aspect of the electron beam. The electron bunch length at the low energy should be measured to study the emittance evolution. The bunch length will be measured by the method of the coherent transition radiation (CTR) with an interferometer in the infrared region. The bunch length optimization to study the emittance oscillation will be also necessary.

6.2.2 Issues of the Stability of Photocathode RF Gun

The timing stability between the laser and the master oscillator is one of the very important issues of the photo-injector. It should be very stable less than 0.1 ps peak to peak. At the same time, the RF power source such as the klystron and the modulator should also be stable. The stability of the power supply for the solenoid, the spectrometer, and the steering magnet should be improved as well.

REFERENCES

- [1] TESLA, Conceptual Design Report, DESY, Hamburg, 1997.
- [2] LCLS, Conceptual Design Report, SLAC-R-593, SLAC, Stanford, 2002.
- [3] SCSS XFEL R&D Group, Conceptual Design Report, SCSS XFEL Report, 2005.
- [4] J. S. Oh, D. E. Kim, E. S. Kim, S. J. Park, H. S. Kang, T. Y. Lee, T. Y. Koo, S. S. Chang, C. W. Chung, S. H. Nam, and W. Namkung, "0.3-nm SASE-FEL at PAL," *Nucl. Instr. and Meth.*, **A528**, p. 582, 2004.
- [5] T.-Y. Lee, Y. S. Bae, J. Choi, J. Y. Huang, H. S. Kang, M. G. Kim, D. H. Kuk, J. S. Oh, Y. W. Parc, J. H. Park, S. J. Park, and I. S. Ko, "Design and Physics Issues of the PAL-XFEL," *J. Korean Phys. Soc.*, **48**, p. 791, 2006.

REFERENCES

- [6] PAL 4th Generation Light Source, Conceptual Design Report, Pohang Accelerator Laboratory, Pohang, 2004.
- [7] C. Kim, S. J. Park, J. H. Park, Y. W. Park, J. Y. Huang, J. Choi, and I. S. Ko, "Laser System of Photocathode RF Gun in Pohang Accelerator Laboratory," *Proc. of the ICFA Workshop on Future Light Sources*, Hamburg, Germany, 2006.
- [8] S. J. Park, J. H. Park, Y. W. Parc, C. B. Kim, C. D. Park, J. S. Oh, I. S. Ko, and X. Wang, "Status of PPI (Pohang Photo-Injector) for PAL XFEL," *Proc. of the 2005 Particle Accelerator Conf.*, Knoxville, Tennessee, USA, p. 1734, 2005.
- [9] X. J. Wang, Z. Wu, and H. Ihee, "Femto-seconds Electron Beam Diffraction Using Photocathode RF Gun," *Proc. of the 2003 Particle Accelerator Conf.*, Portland, Oregon, USA, p. 421, 2003.
- [10] J. Cao, Z. Hao, H. Park, C. Tao, D. Kau, and L. Blaszczyk, "Femtosecond Electron Diffraction for Direct Measurement of Ultrafast Atomic Motions," *Appl. Phys. Lett.*, **83**, p. 1044, 2003.
- [11] X. J. Wang, D. Xiang, T. K. Kim, and H. Ihee, "Potential of Femtosecond Electron Diffraction using Near-Relativistic Electrons From a Photocathode RF Electron Gun " *J. Korean Phys. Soc.*, **48**, p. 390, 2006.
- [12] J. B. Hastings, F. M. Rudakov, D. H. Dowell, J. F. Schmerge, J. D. Cardoza, J. M. Castro, S. M. Gierman, H. Loos, and P. M. Weber, "Ultrafast Time-resolved Electron Diffraction with Megavolt Electron Beams," *Appl. Phys. Lett.*, **89**, p. 184109, 2006.
- [13] B. E. Carlsten, "New Photoelectric Injector Design for the Los Alamos National Laboratory XUV FEL Accelerator," *Nucl. Instr. and Meth.*, **A285**, p. 313, 1989.
- [14] D. T. Palmer, "The Next Generation Photoinjector," SLAC-R-500, Ph. D. Thesis, University of Stanford, Stanford, 1998, 132 pp..

REFERENCES

- [15] B. E. Carlsten and M. Ferrario, "Photoinjectors," *Proc. of the 1999 ICFA Workshop on Future Light Sources*, Argonne, Illinois, USA, 1999.
- [16] C. Travier, "High-Brightness Photocathode Electron Sources," LAL-RT 94-15, Linear Accelerator Laboratory, Orsay, France, 1994.
- [17] M. Ferrario, J. E. Clendenin, D. T. Palmer, J. B. Rosenzweig, and L. Serafini, "HOMDYN Study for the LCLS RF Photo-Injector," SLAC-PUB-8400, SLAC, Stanford, 2000.
- [18] B. E. Carlsten, and D. T. Palmer, "Enhanced Emittance Compensation in a High-Frequency RF Photoinjector Using RF Radial Focusing," *Nucl. Instr. and Meth.*, **A425**, p. 37, 1998.
- [19] D. T. Palmer, R. H. Miller, H. Winick, X. J. Wang, K. Batchelor, M. Woodle, and I. Ben-Zvi, "Simulations of the BNL/SLAC/UCLA 1.6 Cell Emittance Compensated Photocathode RF Gun Low Energy Beam Line," *Proc. of the 1995 Particle Accelerator Conf.*, p. 2432, 1995.
- [20] E. L. Saldin, E. A. Schneidmiller, and M. V. Yurakov, *The Physics of the Free Electron Lasers*, Springer-Verlag, Berlin, 1999, 353 pp.
- [21] K.-J. Kim and Z. Huang, *Lecture Note on High-gain FELs*, 2003, 32 pp.
- [22] K.-J. Kim, "RF and Space-Charge Effects in Laser -Driven RF Electron Guns," *Nucl. Instr. and Meth.*, **A275**, p. 201, 1989.
- [23] L. Serafini and J. B. Rosenzweig, "Envelope Analysis of Intense Relativistic Quasilaminar Beams in RF Photoinjectors: A Theory of Emittance Compensation," *Phys. Rev.*, **E55**, p. 7565, 1997.
- [24] S. G. Anderson and J. B. Rosenzweig, "Nonequilibrium Transverse Motion and

REFERENCES

- Emittance Growth in Ultrarelativistic Space-Charge Dominated Beams," *Phys. Rev. ST Accel. Beams*, **3**, p. 094201, 2000.
- [25] F. J. Sacherer, "RMS Envelope Equations with Space Charge," *IEEE Trans. Nucl. Sci.*, **NS-18**, p. 1105, 1971.
- [26] P. M. Lapostolle, "Possible Emittance Increase Through Filamentation Due To Space Charge In Continuous Beams," *IEEE Trans. Nucl. Sci.*, **NS-18**, p. 1101, 1971.
- [27] M. G. Minty and F. Zimmermann, *Measurement and Control of Charged Particle Beams*, Springer-Verlag, New York, 2003, 12 pp.
- [28] T. Wangler, *Principles of RF linear accelerators*, John Wiley & Sons Inc., New York, 1998, 130 pp.
- [29] S. Y. Lee, *Accelerator Physics*, World Scientific Publishing Co., Singapore, 1999, 54 pp.
- [30] K. Flottmann, "Pepper Pot Design for Space Charge Dominated High Brightness Beams," TESLA-FEL 96-09, DESY, Hamburg, 1996.
- [31] X. J. Wang, M. Babzien, R. Malone, and Z. Wu, "Mg Cathode and Its Thermal Emittance," *Proc. of LINAC 2002*, Gyeongju, Korea, p.142, 2002.
- [32] W. S. Graves, L. F. DiMauro, R. Heese, E. D. Johnson, J. Rose, J. Rudati, T. Shaftan, and B. Sheehy, "Measurement of Thermal Emittance for a Copper Photocathode," *Proc. of the 2001 Particle Accelerator Conf.*, Chicago, Illinois, USA, p. 2227, 2001.
- [33] J. H. Billen and L. M. Young, "POISSON/SUPERFISH", Los Alamos National Laboratory, Los Alamos, 1996.

REFERENCES

- [34] L. M. Young, "PARMELA Ver.7.14", Los Alamos National Laboratory, Los Alamos, 1996.
- [35] R. Bossart, J. C. Godot, H. Kugler, J. H. B. Madsen, A. Riche, and J. Ströde, "RF-Gun Construction, Tuning and High Power Tests," *Proc. of the 1992 European Particle Accelerator Conf.*, Berlin, Germany, p. 1026, 1992.
- [36] The MAFIA collaboration, "User's Guide MAFIA," CST GmbH, Germany.
- [37] Ansoft Corporation, <http://www.ansoft.com/>
- [38] J. Gao, "Analytical Formulas for the Resonant Frequency Changes due to Opening Apertures on Cavity Walls," *Nucl. Instr. and Meth.*, **A311**, p. 437, 1992.
- [39] J. Gao, "Analytical Formula for the Coupling Coefficient β of a Cavity Waveguide Coupling System," *Nucl. Instr. and Meth.*, **A309**, p. 5, 1991.
- [40] Edward L. Ginzton, *Microwave Measurements*, Acta Crystallographica, 1958, 314 pp.
- [41] A. Chao and M. Tigner, *Handbook of Accelerator Physics and Engineering*, World Scientific Publishing, Singapore, 1999, 404 pp.
- [42] H. Padamsee, J. Knobloch, and T. Hays, *RF Superconductivity for Accelerators*, John Wiley & Sons Inc., New York, 1998, 43 pp.
- [43] S. J. Park, S. H. Kim, Y. J. Park, J. S. Oh, S. H. Nam, C. H. Chung, M. H. Cho, and W. Namkung, "Development of a High-Power Klystron for Radio-Frequency Linear Accelerators," *J. Korea Phys. Soc.*, **48**, p. 786, 2006.
- [44] John G. Power, "Slit Scattering Effects in a Well Aligned Pepper Pot," *Proc. of the 2003 Particle Accelerator Conf.*, Portland, Oregon, USA, p. 2432, 2003.

REFERENCES

- [45] A. Vignati and F. Sannibale, "A Pepper-pot Emittance Meter for Low-energy and High-current Electron Beams," *Nucl. Instr. and Meth.*, **B66**, p. 503, 1992.
- [46] C. H. Wang, M. Clausen, Z. Kakucs, and M. Zhang, "Slits Measurement of Emittance on TTF," *Proc. of the ICALEPCS 1999*, Trieste, Italy, p. 284, 1999.
- [47] J. G. Wang, D. X. Wang, and M. Reiser, "Beam Emittance Measurement by the Pepper-pot Method," *Nucl. Instr. and Meth.*, **A307**, p. 190, 1991.
- [48] Y. Yamazaki, H. K. T. Kurihara, I. Sato, and A. Asarni, "High-precision Pepper-pot Technique for a Low-emittance Electron Beam," *Nucl. Instr. and Meth.*, **A322**, p. 139, 1992.
- [49] M. Zhang, "Emittance Formula for Slits and Pepper-pot Measurement," FERMILAB-TM-1988, Fermi National Accelerator Laboratory, Batavia, 1996.
- [50] A. Cianchi, L. Catani, M. Boscolo, M. Castellano, A. Clozza, G. Di Pirro, M. Ferrario, D. Filippetto, V. Fusco, L. Giannessi, L. Picardi, L. Quattromini, C. Ronsivalle, and C. R. Frascati, "Design Study of a Moveable Emittance Meter Device for the SPARC Photoinjector," *Proc. of the 9th European Particle Accelerator Conf.*, Switzerland, p. 2622, 2004.
- [51] Bergoz Instrumentation, "Integrating Current Transformer User's Manual," Pouilly, France.
- [52] J. Yang, T. Kondoh, Y. Yoshida, and S. Tagawa, "Experimental Studies of Transverse and Longitudinal Beam Dynamics in Photoinjector," *Jpn. J. Appl. Phys.*, **44**, p. 8702, 2005.
- [53] T. Nakajyo, J. Yang, F. Sakai, and Y. Aoki, "Quantum Efficiencies of Mg Photocathode under Illumination with 3rd and 4th Harmonics Nd:LiYF₄ Laser Light in RF Gun," *Jpn. J. Appl. Phys.*, **42**, p. 1470, 2003.

REFERENCES

- [54] X. J. Wang, T. Srinivasan Rao, K. Batchelor, I. Ben-Zvi, and J. Fischer, "Measurements on Photoelectrons from a Magnesium Cathode in a Microwave Electron Gun," *Nucl. Instr. and Meth.*, **A356**, p. 159, 1995.
- [55] D. Xiang, S. J. Park, J. H. Park, Y. W. Parc, and X. J. Wang, "Reduction of Thermal Emittance by using P-Polarized Laser at Oblique Incidence," *Nucl. Instr. and Meth.*, **A562**, p. 48, 2006.
- [56] T. Kobayashi, M. Uesaka, Y. Katsumura, Y. Muroya, T. Watanabe, T. Ueda, K. Yoshii, K. Nakajima, X. Zhu, and M. Kando, "High-Charge S-Band Photocathode RF-Gun and Linac System for Radiation Research," *J. Nucl. Sci. Technol.*, **39**, p. 6, 2002.
- [57] J. W. Wang, "RF Properties of Periodic Accelerating Structures for Linear Colliders," SLAC-R-339, Ph. D. Thesis, University of Stanford, Stanford, 1989, 96 pp..
- [58] A. W. Chao and M. Tigner, *ibid*, 288 pp.
- [59] M. Reiser, *Theory and Design of Charged Particle Beams*, John Wiley & Sons Inc., New York, 1994, 389 pp.
- [60] S. G. Anderson, J. B. Rosenzweig, G. P. LeSage, and J. K. Crane, "Space-charge Effects in High Brightness Electron Beam Emittance Measurements," *Phys. Rev. ST Accel. Beams*, **5**, p. 014201, 2002.
- [61] G. P. Gallerano, A. Doria, E. Giovenale, and G. Messina, "Coherence Effects in FEL Radiation Generated by Short Electron Bunches," *Nucl Instr. and Meth.*, **A358**, p. 78, 1995.
- [62] H. S. Kang, and G. Kim, "Femtosecond Electron Beam Bunch Compression by using an Alpha Magnet and a Chicane Magnet at the PAL Test Linac," *J. Korea Phys. Soc.*, **44**, p. 1223, 2004.

요약문

본 논문은 펨토초 회절현상, 펨토초 원적외선 방사와 X-선 자유전자 레이저등과 같은 장치를 위하여 미국의 브록헤븐 국립연구소와 포항가속기 연구소 간의 공동연구 중인 BNL Gun-IV 형의 고주파 광음극 전자총에 대하여 다룬다. 전자총은 빔 에미턴스 상쇄용 집속 전자석 (solenoid), 빔 진단용 장치와 구리 음극을 가진 1.6 셀(cell)의 공동(cavity)으로 구성된다. 요구되는 2,856 MHz 의 주파수를 제공하기 위해 공동의 2 차원 치수는 SUPERFISH 전산모사 코드를 이용하여 결정되었다. 레이저 입출구, 고주파 결합(coupling)을 위한 도파관 입출구와 진공 펌핑용 입출구 등의 3 차원 주파수 변화량은 Slater 의 섭동이론에 근거하여 계산되었다. 클라이스트론과 고주파 공동사이의 자기적 결합을 위한 도파관 출입구의

치수는 수치적으로 계산 후 절삭과 측정을 반복하면서 결정하였다. 운전 중에 공동의 주파수를 측정하는 방법을 실험적으로 개발하였으며 이를 소개한다. 전자빔 동역학 연구와 전자빔 진단에 필요한 빔 생성을 보장하기 위해 마이크로웨이브 변수들을 측정하였다. 고주파 광음극 전자총 시스템의 성공적인 설치를 확인하기 위한 전자빔 기초 변수들을 측정하였다. 빔 기초 진단변수들은 빔 사이즈, 빔 전하량과 레이저 입사 위상에 따른 전하량 변화, 빔 에너지와 레이저 입사 위상에 따른 에너지 변화와 광음극에서 떨어진 거리에 따른 전자빔 에미턴스의 전개 과정을 포함한다. 광 전자빔 에너지와 전하량의 최대 성능치는 레이저 입사 위상이 30° 일 때 3.7 MeV 와 550 pC 으로 각각 측정되었다. 또한 빔의 사이즈와 에미턴스의 최대 성능치는 레이저 입사 위상 30° 일 때 300 pC 의 전하량을 가진 3.7 MeV 전자빔에서 0.79 ± 0.042 mm 와 1.72 ± 0.29 mm-mrad 로 각각 측정되었다. 추가적인 실험에서 고주파 광음극 전자총의 성공적인 성능 확인을 위해 에미턴스의 전개과정에 대한 실험을 에미턴스 메터를 이용하여 수행하였다. 이 실험을 통하여 에미턴스를 상쇄시켜 최소의 빔 에미턴스를 달성하기 위한 실험적 조건들이 제시되었다. 위의 에미턴스 전개과정의 실험결과와 전산모사 간에는 상당한 일치되는 결과를 보였다. 본 논문에서 에미턴스 전개 과정과 에미턴스 상쇄에 대한 전산모사적 접근과 실험적 접근에 관하여 논의하였다.

Curriculum Vitae

PERSONAL INFORMATION

- Name: Jangho Park
- Date of Birth: 27 June 1974
- Address:
Department of Physics, POSTECH
San-31, Hoyja-dong, Nam-gu,
Pohang, Kyung-Buk, 790-784
Republic of Korea
- E-Mail: wpjho@postech.ac.kr

EDUCATION

Doctorate of Philosophy, in Accelerator Physics, February, 2007
Pohang University of Science and Technology, Pohang, 790-784, Korea
Dissertation: Emittance Evolution Process in High Brightness Photo-Cathode RF Gun with Focusing Solenoids
Adviser: Prof. In Soo Ko

Master of Science, Physics, February 2003
Pohang University of Science and Technology, Pohang, 790-784, Korea
Thesis: Studies of Polarized Electron Source at Pohang Accelerator Laboratory

Bachelor of Science, Physics, February 2001
Kumoh National Institute of Technology (KIT), Gumi, 730-701, Korea
Early Graduation of Superior in the 3rd year

RESEARCH EXPERIENCES

Research Student

Development Group of Accelerator Division
Pohang Accelerator Laboratory (PAL/POSTECH), Pohang, 790-784, Korea
March 2002 – Present

- (1) Developed and constructed photo-cathode rf gun for FIR and PAL-XFEL to investigate beam dynamics in the photo-injector.
- (2) Operated and studied photo-cathode rf gun for basic beam diagnostics and advanced beam experiment such as femto-second electron diffraction and Compton scattering.
- (3) Designed and measured all rf parameters of rf gun cavity using various simulation code and network analyzer.

Research Assistant / Ph.D. Research

Department of Physics
Pohang University of Science and Technology, Pohang, 790-784, Korea
March 2002 – Present

Research Advisor: Prof. In Soo Ko

- (1) Developed and constructed photo-cathode rf gun facility to investigate beam dynamics in the gun for femto-second far infrared radiation and PAL XFEL.
- (2) Developed and constructed slit-based Emittance-Meter to investigate beam dynamics in the photo-injector.
- (3) Developed and studied a p-doped Ga-As based polarized electron source.

Research Participant for Project

Pohang University of Science and Technology, Pohang, 790-784, Korea

March 2006 – Present

P.I.: Prof. In Soo Ko

Researched the roles of beam generation and operations of low emittance electron beam generation for femto-second electron beam diffraction.

Research Participant for Project

Pohang Accelerator Laboratory (PAL/POSTECH), Pohang, 790-784, Korea

September 2002 – July 2006

P.I.: Dr. Sungju Park

Research roles of beam diagnostics of Proton Engineering Frontier Project.

RESEARCH INTERESTS

- Developing and utilizing a semiconductor based multi-bunch photo-cathode rf gun for ILC and XFEL.
- Beam dynamics measurement in the photo-injector for emittance compensation using a slit-based Emittance-Meter.
- Bunch length measurement in the photo-cathode gun with low charge and low energy for femto-second electron diffraction using coherent transition radiation.
- Developing a polarized electron source.

SKILLS

Experimental Experiences

- Developed and constructed photo-cathode rf gun facility to investigate the beam dynamics in the gun for femto-second far infrared radiation and PAL XFEL:
 - RF gun cavity designs using SUPERFISH, PARMELA, HFSS, and Microwave Studio code.
 - RF parameters of fabricated gun cavity measure using network analyzer with tuning method.
 - Photo-cathode rf gun operate for beam dynamics experiments.
- Developed and constructed slit based Emittance-Meter for emittance evolution measurement in the photo-injector region:
 - Developed Emittance-Meter for study of emittance evolution in the photo-injector.
 - Developed and constructed various beam diagnostic system such as integrated current transformer (ICT), Faraday cup, charge coupled device camera, and coherent transition radiation (CTR).
 - Constructed spectrometer magnet for beam energy measurement.
- Developed and constructed proton beam diagnostics system for Proton Engineering Frontier Project:
 - Developed and constructed 4-button type beam position monitor using MAGIC code simulation.
 - Developed and constructed DCCT, Tuned CT, and ICT for proton beam current measurements.
- Developed and studied polarized electron source:
 - Measured quantum efficiency and polarization of p-doped Ga-As electron source.
 - Composed of ultra high vacuum chamber with polarized electron source, electro static bender, and Mott polari-meter, and channel electron multiplier.

- Experimented in using the instruments and equipment:
 - Network Analyzer for measuring the rf parameters of rf gun cavity.
 - DG535 for timing synchronization between a laser beam and an rf power.
 - Sampling oscilloscope and general oscilloscope.
 - Various vacuum devices for the preparation of ultra high vacuum chambers.
 - Various power supplies for magnets and solenoids.

Teaching Experiences

- Global Leadership School, Handong Global University, Pohang, 791-708, Korea,
March 2004 – August 2004
Lecture for “General Physics” of undergraduate course
- Dept. of Physics, POSTECH, Pohang, 790-784, Korea,
September 2003 – February 2004
Teaching assistant for “Electrodynamics II” of graduate course
- Dept. of Physics, POSTECH, Pohang, 790-784, Korea,
March 2001 – February 2002
Teaching assistant for “Experiments of General Physics” of undergraduate course

Other Activities

- Participant, International Accelerator School for Linear Colliders
May 19 - 27, 2006, Sokendai, Hayama, Japan
- Staff Secretariat, ICALEPCS 2003
October 13 - 17, 2003, Gyeongju, Korea
- Editor, 21st Linear Accelerator Conference
August 19 - 23, 2002, Gyeongju, Korea

Honors and Awards

- Award of Superior Student at Graduation Ceremony in KIT, 2001
Gumi Mayor Award, Gumi, Korea
- Honor Student, March, 1998 – February, 2001
Kumoh National Institute of Technology (KIT), Gumi, 730-701, Korea

PUBLICATIONS

International Journals

1. Dao Xiang, Sung-Ju Park, **Jang-Ho Park**, Yong-Woon Parc, and X. J. Wang, "Reduction of Thermal Emittance by using P-polarized Laser at Oblique Incidence", *Nucl. Insrt. and Meth.*, **A562**, p. 48, 2006.
2. T.-Y. Lee, Y. S. Bae, J. Choi, J. Y. Huang, H. S. Kang, M. G. Kim, D. H. Kuk, J. S. Oh, Y. W. Parc, **J. H. Park**, S. J. Park and I. S. Ko., "The Design and Physics issues of PAL XFEL", *J. Korea Phys. Soc.*, **48**, p. 791, 2006.
3. **J. H. Park**, S. J. Park, I. S. Ko, M. H. Cho, W. Namkung, G. Kim, D. Son, "Studies of the test Stand of the Polarized Electron Cathode at the Pohang Accelerator Laboratory", *J. Korea Phys. Soc.*, **44**, p. 1303, 2004.
4. **J. H. Park**, S. J. Park, C. B. Kim, J. H. Hong, J. Y. Huang, D. Xiang, X. J. Wang, and I. S. Ko, "High Power Beam Test and Emittance Evolution of a Photocathode RF Gun at Pohang Accelerator Laboratory", *Japanese Journal of Applied Physics*, accepted (2006).
5. C. Kim, S. J. Park, **J. H. Park**, Y. W. Parc, J. Y. Huang, J. Choi, and I. S. Ko, "Laser System of Photocathode RF Gun in Pohang Accelerator Laboratory," *J. Korea Phys. Soc.*, accepted (2006).

6. **J. H. Park**, S. J. Park, In Soo Ko et al., "High Power RF Characteristics of a 1.6-Cell RF Gun Cavity at Pohang Accelerator Laboratory", *J. Korea Phys. Soc.*, submitted (2006).
7. Y. W. Park, S. J. Park, C. B. Kim, **J. H. Park**, J. H. Huang, I. S. Ko, *J. Korea Phys. Soc.*, submitted (2006).

International Proceedings

1. **J. H. Park**, S. J. Park, and I. S. Ko et al., "Preliminary Measurement of Emittance Evolution Using Emittance Meter at the PAL," *Proc. of the 28th International Free Electron Laser Conference* (2006).
2. **Jangho Park**, Sung-Ju Park et al., "Performance Test of RF Photo-cathode Gun at The PAL," *Proc. of the 2006 European Particle Accelerator Conference* (2006).
3. Changbum Kim, Sung-Ju Park, **Jangho Park**, et al., "Laser System of Photocathode RF Gun at Pohang Accelerator Laboratory," *Proc. of the 2006 Future Light Sources Workshop* (2006).
4. S. J. Park, **J. H. Park**, et al., "Physics and Engineering Issues of PPI (Pohang Photo-Injector) for PAL XFEL," *Proc. of the 27th International Free Electron Laser Conference* (2005).
5. Sung-Ju Park, **Jangho Park**, et al., "Status of beam diagnostic Systems for the PEPF," *Proc. of the 2005 Particle Accelerator Conference* (2005).
6. Sung-Ju Park, **Jangho Park**, et al., "Status of PPI (Pohang Photo-Injector) for PAL XFEL," *Proc. of the 2005 Particle Accelerator Conference* (2005).
7. **Jangho Park**, Sung-Ju Park, et al., "Measurements of Transverse Emittance for RF Photocathode Gun at The PAL," *Proc. of the 2005 Particle Accelerator Conference* (2005).
8. S. J. Park, J. S. Oh, E. S. Kim, J. Y. Huang, D. E. Kim, **J. H. Park**, et al., "Design Study of Low-Emittance Injector for SASE XFEL at Pohang

- Accelerator Laboratory,” *Proc. of the 2004 Free Electron Laser Conference* (2004).
9. S .J. Park, **J. H. Park**, et al., “Developmental Status of Beam Position and Phase Monitor for PEFP Proton Linac,” *Proc. of the 2004 Beam Instrumentation Workshop* (2004)
 10. S. J. Park, **J. H. Park**, et al., “Developmental Status of PEFP/KAERI Beam Diagnostic System,” *Proc. of the 2004 Asian Particle Accelerator Conference* (2004).
 11. S. J. Park, **J. H. Park** et al., “Beam Diagnostic System for High Intensity Proton Linac at KAERI,” *Proc. of the 2003 Particle Accelerator Conference* (2003).
 12. S. J. Park, **J. H. Park**, et al., “Design of BPM PU for Low-beta Proton Beam Using Magic Code”, *Proc. of DIPAC 2003* (2003)